

Reconstruction Algorithms for Computed Tomography

CLAAS BONTUS AND THOMAS KÖHLER

*Philips Research Europe–Hamburg, Sector Medical Imaging Systems,
Röntgenstrasse 24–26, D-22 335 Hamburg, Germany*

I. Introduction	2
II. Principles of Computed Tomography	4
A. X-Ray Attenuation	4
B. Parameterization of the Measurements	5
1. Field of View and Region of Interest	6
C. Detector Shapes	7
1. Basis Vectors	10
D. Trajectories	10
1. Circular Trajectory	10
2. Helical Trajectory	12
III. CT Reconstruction	15
A. Radon Transform	15
1. Inverse Radon Transform	16
2. Fourier Slice Theorem	18
B. Exact Filtered Backprojection	19
1. Derivative of the Projection Data	19
2. Reconstruction Formula	20
3. Mathematically Complete Trajectories	23
4. Reconstruction Algorithm	24
5. Filtering	25
6. Efficient Filtering	27
7. Backprojection Using Wedge Detector Geometry	31
C. Mathematics on the Planar Detector	32
D. Circle Plus Line	34
1. Geometrical Properties	35
2. Filter Lines	36
3. Proof of Exactness	38
4. Reconstruction Results	40
E. The Katsevich Algorithm for Helical Pi Acquisition	42
1. Geometrical Properties	42
2. Filter Lines	43
3. Proof of Exactness	46
F. <i>EnPiT</i> : Helical n -Pi Reconstruction	49
1. Reconstruction Algorithm	50
2. Filter Lines	51
G. <i>CEnPiT</i> : Helical Cardiac CT	52
1. Cardiac CT	52
2. Filter Lines	56

3. Gated and Ungated Contributions	58
IV. Outlook	59
References	61

I. INTRODUCTION

Computed tomography (CT) is of vital importance for medical diagnosis, intervention planning, and treatment evaluation. CT yields three-dimensional (3D) tomographic images of large parts of the human body within a few seconds. The rather wide bore allows use of CT scans for obese patients and claustrophobia is rarely an issue. At the same time, the current pace of technological progress is unprecedented. Two major advances are important. First, X-ray detectors are larger, allowing scanning larger volumes in shorter times. Second, rotation speeds of the tube-detector system are steadily increasing.

Although the technological progress is of great benefit for patients and medical staff, the engineering challenges are great. X-ray tubes must be able to withstand the centrifugal forces increasing with the rotation speed. These tubes also must be able to illuminate detectors of increasing sizes. Integration times of the detector elements become shorter. The amount of data measured per time unit increases with increasing rotation speed and detector sizes. All these data must be transmitted and processed in an appropriate amount of time.

Data processing is separated into different steps: preprocessing, reconstruction and image processing. Preprocessing covers correction methods to treat disturbing effects and system imperfections, such as beam hardening, cross-talk, and afterglow. For example, beam hardening is a nonlinear effect resulting from the fact that X-rays experience weaker absorption with increasing photon energy. Image-processing methods cover all algorithms that are applied to the image data to assist radiologists in image analysis. Examples for image-processing methods are tools that automatically segment different organs, as well as computer-aided diagnosis (CAD) tools.

This chapter covers the field of CT reconstruction, i.e., the mathematics to obtain the image data from the measurements. In other words, reconstruction deals with an inverse problem. Reconstruction algorithms must fulfill certain criteria to be useful in practice. They must be numerically stable and yield images of sufficient quality with respect to artefacts, resolution, and signal to noise ratio (SNR). Furthermore, reconstruction algorithms should be sufficiently fast so that images can be obtained in an adequate amount of time.

Historically, most CT scanners were so-called single-row scanners. These scanners yield two-dimensional (2D) images of cross-sectional slices. The

mathematics for single-row scanners is well understood. Modern cone-beam CT scanners, in which the detector consists of many rows, require completely new reconstruction algorithms. The first reconstruction algorithms proposed for cone-beam scanners were extensions of 2D methods. These algorithms, which are of approximative nature, yield good image quality as long as the number of detector rows does not become too large. Once the number of rows becomes large, more effort is necessary and the underlying mathematics must be analyzed to develop more sophisticated algorithms.

In 2002 Alexander Katsevich (2002) published the first reconstruction algorithm for helical CT, which is mathematically exact, of the filtered backprojection (FBP) type, and in which the filtering is shift invariant. In particular, the exactness guarantees that remaining artefacts originate from the discrete reformulation of the inversion formulas. This discretization is required by the discrete sampling of the projection data. FBP, in combination with the shift invariance of the underlying filter, ensures that the algorithm can be implemented in an efficient way. Katsevich's work resulted in many publications analyzing the underlying mathematics or extending the algorithm to different settings.

The chapter is devoted to reconstruction algorithms of the FBP type that are derived from an exact method. The underlying mathematics is discussed on a broad basis. Nevertheless, more effort is placed on descriptive discussions than on waterproof mathematical analyses. Section II provides a short summary of the principles. The measurement process as well as different kinds of detectors and trajectories are discussed. Section III covers the field of reconstruction in several subsections, beginning with the Radon transform in Section III.A. As it turns out, the mathematics associated with the discussed algorithms can be separated into two parts. While Sections III.B and III.C deal with the formulas that are independent of the particular system settings, the subsequent sections specify the parameters for different types of acquisitions. The mathematics of the circle and line trajectory (CLT) can be understood readily. This trajectory, therefore, serves as the first example, covered in Section III.D. The Katsevich algorithm for a so-called Pi acquisition is covered in Section III.E, while Section III.F deals with the so-called *EnPiT* algorithm. The *EnPiT* algorithm can be considered an extension of the Katsevich method useful for more freely choosing the patient table feed. Cardiac CT is one of the most important applications for modern CT scanners. The *CEnPiT* algorithm, which was developed for cardiac cone-beam CT based on a helical acquisition, is briefly summarized in Section III.G.

II. PRINCIPLES OF COMPUTED TOMOGRAPHY

A. X-Ray Attenuation

Figure 1 shows a modern CT scanner. Within such a CT system a tube emits X-rays in the direction of a detector. The X-rays penetrate a certain part of the patient's body before they enter the detector. During the scan the tube-detector system (termed as the *gantry*) rotates around the patient (see Figure 2) so that projections from a large number of directions are taken. The patient lies on a patient table, that can be moved during the scan. In this manner, a relative motion of the patient with respect to the rotation plane can be realized. In practice, this is used, for example, to obtain a relative trajectory in which the X-ray tube moves on a helix around the patient.

Consider the X-ray tube itself. Let us denote the flux density of X-ray photons with energy E emitted into a certain direction by $I_0(E)$. Typical units for the photon flux density are $[I] = 1/\text{s sr keV}$; that is $I(E)$ is the number of photons emitted within each second per solid angle and per photon energy. Some X-ray photons are scattered or absorbed when penetrating the patient. The number of photons, that pass through the patient (not scattered and not absorbed) is given by the Beer–Lambert law:

$$I(E) = I_0(E) \exp\left(-\int d\ell \mu(\mathbf{x}(\ell), E)\right). \quad (1)$$



FIGURE 1. The Philips Brilliance 64 is a modern CT scanner with 64 detector rows.

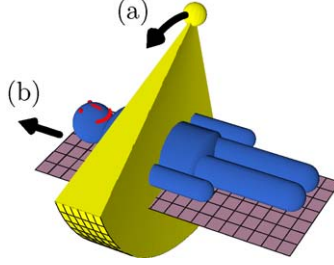


FIGURE 2. (a) The tube-detector system rotates around the patient during a CT scan. (b) The patient table can be moved so that a helical trajectory can be realized.

Here, $\mathbf{x}(\ell)$ parameterizes the path along which the X-rays travel. The scalar function $\mu(\mathbf{x})$ are the so-called absorption coefficients. Function $\mu(\mathbf{x})$ is also known as the *object function*. Certainly, the values of μ are different for different kinds of tissue.

The aim of reconstruction is to recover the μ -values from the measurements.

From Eq. (1) we easily obtain

$$\int d\ell \mu(\mathbf{x}(\ell), E) = \ln(I_0(E)/I(E)). \quad (2)$$

In other words, a monochromatic CT system measures line integrals. Unfortunately, X-rays emitted from today's tubes have a wide spectrum and the detectors average over the photon energies. Therefore, some preprocessing steps are necessary before the measurements can approximately be interpreted as line integrals.

B. Parameterization of the Measurements

The following sections assume that the preprocessing steps yield data, which can be interpreted as line integrals in the sense of Eq. (2) with $E = E_0$, where E_0 is some mean energy. We choose a coordinate system, which is fixed to the patient. At a particular time the X-ray source will be at a point \mathbf{y} with respect to this coordinate system. The line integrals associated with the measurements at this point in time all originate from \mathbf{y} . Terms *source position* and *focal spot* are used synonymously throughout this chapter and correspond to vectors \mathbf{y} .

Each line integral can be parameterized as

$$D(\mathbf{y}, \boldsymbol{\theta}) = \int_0^{\infty} d\ell \mu(\mathbf{y} + \ell \boldsymbol{\theta}), \quad (3)$$

where $\boldsymbol{\theta}$ is a unit vector pointing into the direction of the line integral. The different values of $\boldsymbol{\theta}$ are determined by the locations of the different detector elements.

If the patient table is fixed during the scan (see [Figure 2](#)), the source moves on a circular trajectory with respect to the coordinate system defined above. This trajectory can be parameterized as

$$\mathbf{y}_o(s) = \begin{pmatrix} R \cos s \\ R \sin s \\ z_0 \end{pmatrix}, \quad (4)$$

where R corresponds to the distance from the source to the rotation axis. We use the angular variable s to parameterize points on the trajectory. Each measurement belongs to a certain s . The set of measured values, i.e., all detector values, belonging to a certain s is denoted as a projection.

For a helical trajectory, the positions of the source can be described with the help of the vector

$$\mathbf{y}_H(s) = \begin{pmatrix} R \cos s \\ R \sin s \\ s\hbar \end{pmatrix}, \quad (5)$$

where $h = 2\pi\hbar$ corresponds to the pitch—the table feed per rotation. Finally, a line parallel to the z -axis is given by

$$\mathbf{y}_|(z) = \mathbf{y}_|(hs) = \begin{pmatrix} R \\ 0 \\ z \end{pmatrix}, \quad (6)$$

where h is an arbitrary constant, which was introduced to make \mathbf{y} depend on the angular variable s . A linear trajectory according to Eq. (6) can be realized if the tube-detector system does not rotate but the patient table moves (compare with [Figure 2](#)).

1. Field of View and Region of Interest

As discussed above, the aim of CT reconstruction is to recover the absorption coefficients μ from the measurements. The question of whether a certain object point \mathbf{x} is reconstructible—if its μ value can be determined—is of particular interest. This question is related to the set of directions from which \mathbf{x} is illuminated by X-rays. The set of all object points, which are

reconstructible, is denoted as the *field of view* (FOV). The *region of interest* (ROI) is the set of all object points the user wants to be reconstructed. Some approximate algorithms yield absorption coefficients even for object points that do not belong to the FOV. These algorithms provide good approximation for object points that are not reconstructible in a strict sense. In other words, the ROI can be a subset or a superset of the FOV.

C. Detector Shapes

Detectors in conventional CT scanners are so-called focus-centered detectors. These detectors have a cylindrical shape such that the symmetry axis of the cylinder is parallel to the z -axis and contains the focal spot. The focal spot is the point within the X-ray tube from which the X-rays originate. Points on the focus detector are parameterized using the fan-angle variable φ and the coordinate v_F as shown in Figure 3. Our conventions are such that the point ($\varphi = 0$, $v_F = 0$) corresponds to the center of the detector. Physical detectors consist of detector elements, such that the detector coordinates used to describe the measurements take only discrete values. In particular, these values are

$$\varphi_k = \varphi_0 + k\Delta\varphi, \quad k = 0, \dots, \#\text{columns} - 1, \quad (7)$$

$$v_{Fp} = v_{F0} + p\Delta v, \quad p = 0, \dots, \#\text{rows} - 1, \quad (8)$$

which defines the notion of detector columns and rows.

For convenience we introduce two virtual detectors—the planar and the parallel (wedge) detector. Data on these virtual detectors can be obtained by rebinning steps using the focus-detector data. In our convention, the planar

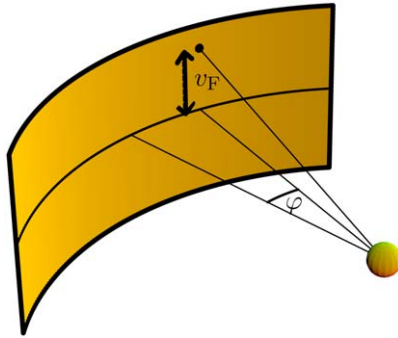


FIGURE 3. Points on the focus-centered detector are parameterized by the fan-angle variable φ and coordinate v_F .

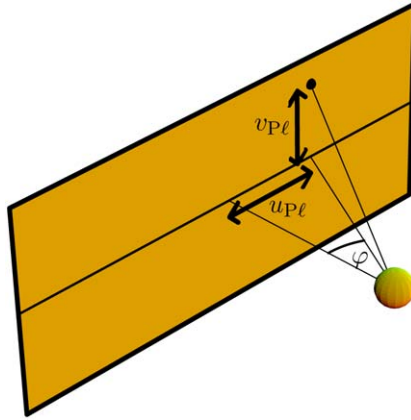


FIGURE 4. Points on the planar detector are parameterized by the variables $u_{P\ell}$ and $v_{P\ell}$.

detector contains part of the rotation axis. Points on the planar detector are parameterized using the coordinates $u_{P\ell}$ and $v_{P\ell}$ as shown in Figure 4. Focus- and planar-detector coordinates are related by

$$u_{P\ell} = R \tan \varphi \quad (9)$$

and

$$v_{P\ell} = \sqrt{R^2 + u_{P\ell}^2} \tan \lambda = R \frac{\tan \lambda}{\cos \varphi} = \frac{v_F}{\cos \varphi} \frac{R}{D}, \quad \tan \lambda = \frac{v_F}{D}, \quad (10)$$

where D is the distance from the source to the center of the focus detector, and λ is the cone angle.

The wedge detector is illustrated in Figure 5. It has an extended source. In particular, from each source position along the circle or helix, only data from one virtual focus-detector column enter into a wedge-detector projection. A virtual column is a column located somewhere between physical columns. Data along the virtual column can be obtained by interpolation of data from physical columns. For a helical trajectory the wedge detector is *bent* along the z -direction; that is its lower and upper boundaries have the slope of the helix. Details are provided in the following text.

The wedge detector coordinates are designated as u_{\parallel} and v_{\parallel} , as shown in Figure 6. Furthermore, we parameterize different wedge-detector projections by the angular variable t similar to s , which parameterizes different focus-detector projections [compare with Eqs. (4) and (5)]. In particular, t is the angle enclosed by the parallel fans shown in Figure 5 and the x -axis. The angle φ is measured in a plane parallel to the xy -plane. Therefore, the line

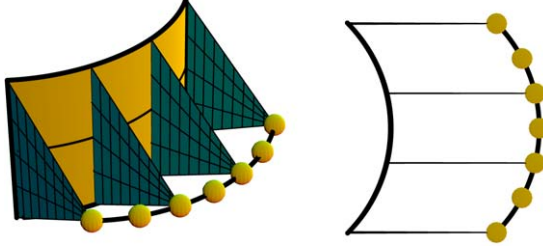


FIGURE 5. For the parallel (wedge) detector data from different source positions must be combined. Data belonging to a particular column of the wedge detector originate from one column of the focus detector at a specific source position. The right image shows the wedge detector on the left seen from above.

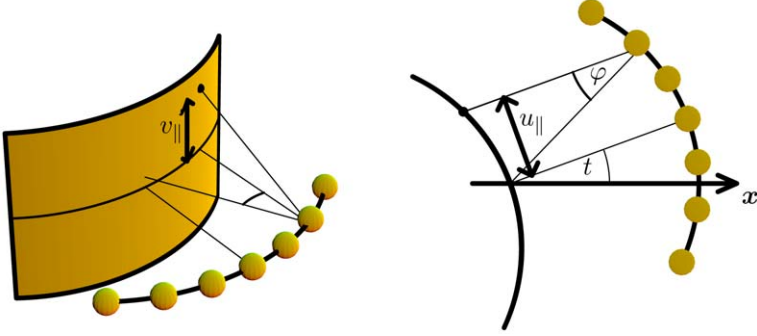


FIGURE 6. Points on the wedge detector are parameterized by the variables $u_{||}$ and $v_{||}$.

(intersecting with the rotation axis) used to measure that angle in Figure 6 does not intersect with the center of the wedge detector.

The relationships between focus- and wedge-detector coordinates are

$$s = t + \varphi, \quad (11)$$

$$u_{||} = R \sin \varphi \quad (12)$$

and

$$\tan \lambda = \frac{v_F}{D} = \frac{v_{||}}{R}. \quad (13)$$

These equations should be interpreted as follows. For given coordinates $(t, u_{||}, v_{||})$ compute φ according to Eq. (12). Now, Eq. (11) indicates from which source positions the data must be taken. Finally, the required row on the focus detector can be computed using Eq. (13). Note that our conventions are such that constant $v_{||}$ means constant v_F . In other words, data belonging

to a row of the wedge detector are taken from the same row but different projections of the focus detector. Therefore, when performing the rebinning from focus to wedge data, interpolations are necessary in φ and s but not in v_F . This explains the bending of the wedge detector in the helical case above.

1. Basis Vectors

For the subsequent discussion it is useful to introduce an orthonormal basis, which is stationary on the planar detector. We define basis vectors $\mathbf{u}(s)$, $\mathbf{v}(s)$, and $\mathbf{w}(s)$ such that

$$\mathbf{x} = u_{p\ell}\mathbf{u} + (v_{p\ell} + y_z(s))\mathbf{v} \quad (14)$$

gives the world coordinates of point $(u_{p\ell}, v_{p\ell})$. The term proportional to $y_z(s)$ (which is the z -component of vector \mathbf{y}) in Eq. (14) is necessary, because the center of the planar detector moves with the source along z . A point \mathbf{x} is located on the planar detector (at least if we consider the detector to have infinite extents), if $\mathbf{x} \cdot \mathbf{w} = 0$. In this case, $(u_{p\ell} = \mathbf{x} \cdot \mathbf{u}, v_{p\ell} = \mathbf{x} \cdot \mathbf{v} - y_z(s))$ gives the planar-detector coordinates of \mathbf{x} .

For the cylindrical trajectories given by Eqs. (4) and (5), the explicit form of the basis vectors are

$$\mathbf{u}(s) = \begin{pmatrix} -\sin s \\ \cos s \\ 0 \end{pmatrix}, \quad \mathbf{v}(s) = \begin{pmatrix} 0 \\ 0 \\ 1 \end{pmatrix}, \quad \mathbf{w}(s) = \begin{pmatrix} \cos s \\ \sin s \\ 0 \end{pmatrix}. \quad (15)$$

D. Trajectories

1. Circular Trajectory

Let us have a closer look at the circular trajectory, Eq. (4). For later reference we consider the stereographic projection of the circle onto the planar detector seen from a source at $\mathbf{y}_|(z_1)$, which is not necessarily in the circle plane [compare with Eq. (6)]. The following derivation aims at obtaining Eq. (22). We describe the line containing the focal spot and the point $\mathbf{y}_\circ(s)$ via

$$\boldsymbol{\ell}(s, \lambda) = (1 - \lambda)\mathbf{y}_|(z_1) + \lambda\mathbf{y}_\circ(s) = (1 - \lambda) \begin{pmatrix} R \\ 0 \\ z_1 \end{pmatrix} + \lambda \begin{pmatrix} R \cos s \\ R \sin s \\ z_0 \end{pmatrix}, \quad (16)$$

where λ parameterizes points on the line. See Figure 7 for an illustration. The just-defined line intersects with the planar detector, if

$$0 = \boldsymbol{\ell} \cdot \mathbf{w} = (1 - \lambda_0)R + \lambda_0 R \cos s, \quad (17)$$

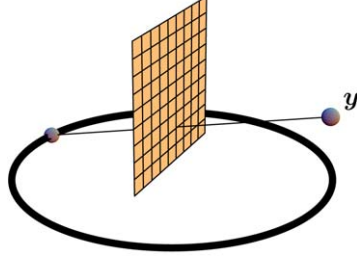


FIGURE 7. The line connecting the focal spot at y and a point on the circle intersects with the planar detector.

where λ_0 parameterizes the point of intersection. In the latter equation \mathbf{w} is the basis vector defined in Section II.C normal to the planar detector. Therefore, $\mathbf{w} = (1, 0, 0)$ in our case. Solving for λ_0 , we obtain

$$\lambda_0 = \frac{1}{1 - \cos s} = \frac{1}{2 \sin^2 s/2}. \quad (18)$$

The planar-detector coordinates of the point of intersection are obtained using basis vectors $\mathbf{u} = (0, 1, 0)$ and $\mathbf{v} = (0, 0, 1)$

$$u_{\text{Pl}}(s) = \boldsymbol{\ell}(s, \lambda_0) \cdot \mathbf{u} = \lambda_0 R \sin s = R \frac{\sin s}{2 \sin^2 s/2} = R \cot \frac{s}{2}, \quad (19)$$

$$v_{\text{Pl}}(s) = \boldsymbol{\ell}(s, \lambda_0) \cdot \mathbf{v} - z_1 = \lambda_0(z_0 - z_1) = \frac{z_0 - z_1}{2 \sin^2 s/2}. \quad (20)$$

These equations are still parameterized by s . We solve Eq. (19) for s . Inserting the result into Eq. (20) and using

$$\sin^2 \arctan \frac{R}{u_{\text{Pl}}} = \frac{R^2}{u_{\text{Pl}}^2 + R^2} \quad (21)$$

provides

$$v_{\text{Pl}}(u_{\text{Pl}}) = \frac{z_0 - z_1}{2} \left(1 + \frac{u_{\text{Pl}}^2}{R^2} \right). \quad (22)$$

The latter equation parameterizes the projection of the circle at $z = z_0$ onto the planar detector as a function of u_{Pl} . For symmetry reasons this equation is valid for all source positions at $z = z_1$ at the surface of the cylinder with radius R .

2. Helical Trajectory

The key for exact reconstruction of helical CT data is the Pi window or Tam–Danielsson window. It is related to the minimum amount of data, that need to be acquired to perform an exact reconstruction (Danielsson *et al.*, 1997; Tam, 1995). The generalization of the Pi window is the so-called n -Pi window, where n is an odd integer (Proksa *et al.*, 2000). Figure 8 depicts the surfaces enclosing the points belonging to the Pi and 3-Pi window associated with a certain source position. These surfaces contain the focal spot and points on the helix. In particular, for the n -Pi window the points on the helix defining the lower surface fulfill the relation

$$s_0 - (n + 1)\pi < s < s_0 - (n - 1)\pi, \quad (23)$$

where s_0 parameterizes the current source position [see Eq. (5)]. Similarly, for the upper surface

$$s_0 + (n - 1)\pi < s < s_0 + (n + 1)\pi. \quad (24)$$

We will now compute the projection of the n -Pi window boundaries onto the planar detector. The derivation is very similar to the treatment of the circular trajectory above. It results in Eq. (32). In particular, the line containing the current source position at $\mathbf{y}_H(s_0)$ and another point on the helix at $\mathbf{y}_H(s)$ is parameterized by

$$\ell(s, \lambda) = (1 - \lambda) \begin{pmatrix} R \cos s_0 \\ R \sin s_0 \\ \hbar s_0 \end{pmatrix} + \lambda \begin{pmatrix} R \cos s \\ R \sin s \\ \hbar s \end{pmatrix}. \quad (25)$$

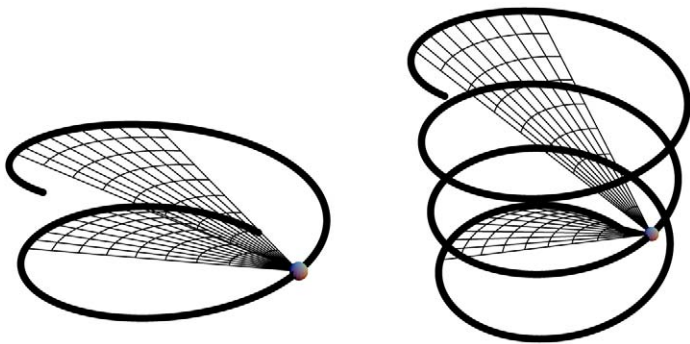


FIGURE 8. Left: The Pi window contains object points enclosed by the shown surfaces. These surfaces contain the focal spot and parts of the helical trajectory. Right: For the 3-Pi window the next-to-next turns of the helix determine the enclosing surfaces.

This line intersects with the planar detector, if

$$0 = \ell(s, \lambda_0) \cdot \mathbf{w}(s_0) = R + \lambda_0 R(\cos \Delta s - 1), \quad \Delta s = s - s_0, \quad (26)$$

where we used the expression for \mathbf{w} in Eq. (15). Solving for λ_0 , we obtain

$$\lambda_0 = \frac{1}{1 - \cos \Delta s} = \frac{1}{2 \sin^2(\Delta s/2)}. \quad (27)$$

Coordinates $u_{P\ell}$ and $v_{P\ell}$ of the point of intersection are obtained via

$$u_{P\ell}(s) = \ell(s, \lambda_0) \cdot \mathbf{u}(s_0) = R \frac{\sin \Delta s}{2 \sin^2(\Delta s/2)} = R \cot \frac{\Delta s}{2}, \quad (28)$$

$$v_{P\ell}(s) = \ell(s, \lambda_0) \cdot \mathbf{v}(s_0) - \hbar s_0 = \frac{\hbar \Delta s}{2 \sin^2(\Delta s/2)}. \quad (29)$$

Now, we introduce angle $\Delta \bar{s}$, such that $\Delta \bar{s} = \Delta s + (n+1)\pi$ for the lower n -Pi window boundary, and $\Delta \bar{s} = \Delta s - (n-1)\pi$ for the upper boundary (compare with Figure 8). Comparing with Eqs. (23) and (24), we realize that $0 < \Delta \bar{s} < 2\pi$. Using $\Delta \bar{s}$ in Eq. (28) and making use of the symmetry of the tan function, we obtain

$$\frac{\Delta \bar{s}}{2} = \operatorname{arccot} \frac{u_{P\ell}}{R}. \quad (30)$$

From Eq. (29) we determine

$$v_{P\ell} = \hbar \left(1 + \left(\frac{u_{P\ell}}{R} \right)^2 \right) \begin{cases} \Delta \bar{s} - (n+1)\pi, & \text{lower boundary,} \\ \Delta \bar{s} + (n-1)\pi, & \text{upper boundary} \end{cases} \quad (31)$$

where we inserted Eq. (30) into the denominator of Eq. (29) and used Eq. (21). Now, using Eq. (30) again and making use of $\operatorname{arccot} u_{P\ell}/R = \pi/2 - \arctan u_{P\ell}/R$, we derive

$$v_{P\ell,n}^{\text{up,low}}(u_{P\ell}) = \pm \hbar \left(1 + \left(\frac{u_{P\ell}}{R} \right)^2 \right) \left(n \frac{\pi}{2} \mp \arctan \frac{u_{P\ell}}{R} \right). \quad (32)$$

The latter equation gives the upper and lower boundaries of the n -Pi window on the planar detector. Figure 9 shows the corresponding curves for cases $n = 1, 3$, and 5 . For later reference, the projections of the lower and upper boundaries of the focus detector result in

$$v_{P\ell\pm}^F(u_{P\ell}) = \pm \frac{H}{2} \sqrt{u_{P\ell}^2 + R^2}, \quad (33)$$

where H is the height of the focus detector.

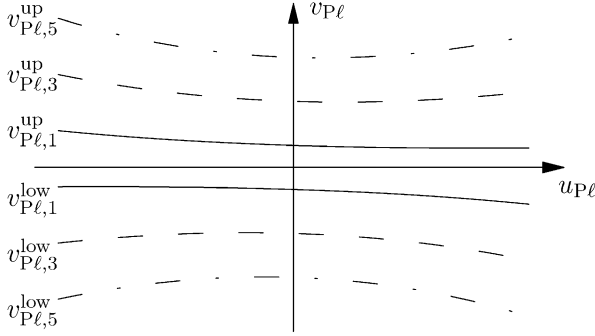


FIGURE 9. The Pi window (solid), 3-Pi window (dashed), and 5-Pi window (dash-dotted) boundaries on the planar detector.

The introduction of the Pi and n -Pi window gives rise to the definition of the Pi and n -Pi segments. These segments are parts of the helix associated with each object point. We start with the Pi segment and consider the projection of a certain object point \mathbf{x} onto the planar detector. From each source position $\mathbf{y}_H(s)$, \mathbf{x} is either projected inside or outside the Pi window. Now, the Pi segment is the union of all points on the helix from which \mathbf{x} is projected into the Pi window. In other words, $\mathbf{y}_H(s)$ belongs to the Pi segment of \mathbf{x} , if

$$v_{P\ell,1}^{\text{low}}(u_{P\ell}) \leq v_{P\ell} \leq v_{P\ell,1}^{\text{up}}(u_{P\ell}).$$

Here, $(u_{P\ell}, v_{P\ell})$ are the coordinates of the projected object point \mathbf{x} , and $v_{P\ell,1}^{\text{low}}$ and $v_{P\ell,1}^{\text{up}}$ are the Pi-window boundaries according to Eq. (32). For each object point two angles s_1 and s_2 can be found, such that $\mathbf{y}_H(s)$ belongs to the Pi segment of \mathbf{x} , if and only if $s_1 \leq s \leq s_2$ (Defrise, Noo and Kudo, 2000). Points $\mathbf{y}_H(s_1)$ and $\mathbf{y}_H(s_2)$ are sometimes denoted as *sunrise* and *sunset*. The three points \mathbf{x} , $\mathbf{y}_H(s_1)$, and $\mathbf{y}_H(s_2)$ are located on a straight line, since \mathbf{x} is projected onto the Pi-window boundary, i.e., onto the helix, from the points of sunrise and sunset (Figure 10). Interval $[s_1, s_2]$ is denoted as the Pi interval of object point \mathbf{x} . The line containing $\mathbf{y}_H(s_1)$ and $\mathbf{y}_H(s_2)$ is called the Pi-line of \mathbf{x} . Obviously, all points located on that line share the same Pi-line and Pi segment.

The situation is similar but slightly more complicated for the n -Pi window. Every point $\mathbf{y}_H(s)$ belongs to the n -Pi segment of \mathbf{x} , if \mathbf{x} is projected between the lower and upper n -Pi window boundaries. Now, for some object points the n -Pi segment is not a single segment. In fact, the n -Pi segment can consist of up to n subsegments. Therefore, some object points experience a sunrise and a sunset up to n times along the helix, a phenomenon known as *interrupted illumination*. See Figure 11 for an example. Similar to the definition of the

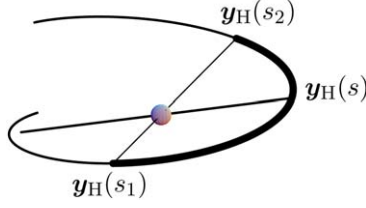


FIGURE 10. The Pi segment of the exemplified object point \mathbf{x} along the helix is printed bold. From each point $\mathbf{y}_H(s)$ within the Pi segment, \mathbf{x} is located between the Pi-window surfaces shown in Figure 8.

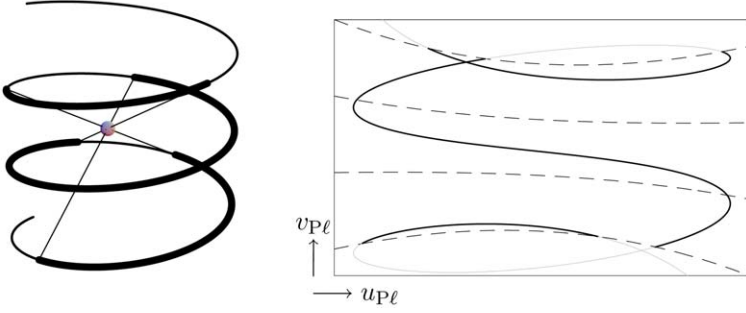


FIGURE 11. Left: The bold points denote the 3-Pi segment of the exemplified object point. Right: Projection of the object point onto the planar detector from different source positions results in the shown trace on the detector. Sunrise or sunset occur if the object point is projected onto the boundaries of the 3-Pi window.

Pi-line, an n -Pi line contains a point of sunrise, a point of sunset, and \mathbf{x} . The number of n -Pi lines can reach the value of n if interrupted illumination occurs.

III. CT RECONSTRUCTION

A. Radon Transform

The Radon¹ transform is an important tool for the analysis and development of reconstruction algorithms. The 3D Radon transform is the set of all plane integrals through a given object function. We parameterize Radon planes by normal vectors $\boldsymbol{\omega}$ and scalars ρ , where ρ is the shortest distance of the plane to the origin (Figure 12). With these conventions the Radon transform of object

¹ Johann Radon, Austrian mathematician, 1887–1956.

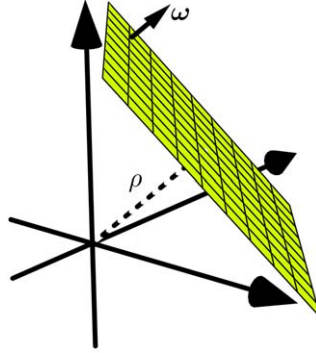


FIGURE 12. An exemplary Radon plane with normal vector ω . The dashed line has the length ρ , which is the shortest distance from the origin to the plane. Points \mathbf{x} on the plane fulfill the relation $\omega \cdot \mathbf{x} = \rho$.

function $\mu(\mathbf{x})$ is given by

$$\mathcal{R}\mu(\rho, \omega) = \int_{-\infty}^{\infty} d^3\mathbf{x} \mu(\mathbf{x}) \delta(\rho - \omega \cdot \mathbf{x}). \quad (34)$$

1. Inverse Radon Transform

The inverse of the Radon transform can be obtained via the following formula (Natterer, 1986)

$$\mu(\mathbf{x}) = \frac{-1}{8\pi^2} \int_0^\pi d\vartheta \int_0^{2\pi} d\alpha \sin \alpha \mathcal{R}'' \mu(\omega \cdot \mathbf{x}, \omega), \quad (35)$$

where

$$\omega = (\cos \alpha \sin \vartheta, \sin \alpha \sin \vartheta, \cos \vartheta) \quad (36)$$

and

$$\mathcal{R}'' \mu(\rho, \omega) = \frac{\partial^2 \mathcal{R}\mu(\rho, \omega)}{\partial \rho^2} \quad (37)$$

is the second derivative of the Radon transform with respect to ρ . The interpretation of Eq. (35) is as follows. In standard convention the (scalar) value associated with one particular Radon plane enters Radon space at point $\rho\omega$. Now, for the evaluation of Eq. (35) all Radon values are taken into account for which $\rho = \omega \cdot \mathbf{x}$, i.e., all Radon planes are considered, which contain \mathbf{x} .

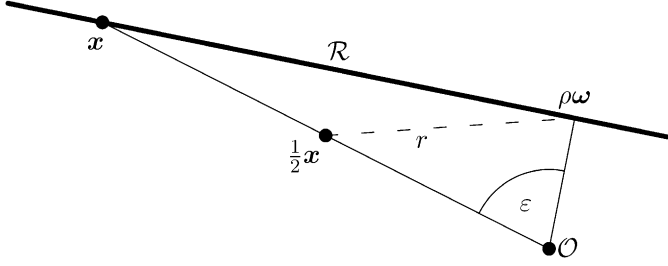


FIGURE 13. Two-dimensional cut parallel to ω and containing x and the origin O . The Radon plane \mathcal{R} is a straight line in this view, since ω is normal to \mathcal{R} .

We show that all Radon values that must have to be taken into account are located on the surface of a sphere in Radon space (Figure 13). This figure shows a 2D cut parallel to ω containing x and the origin O . The Radon plane \mathcal{R} defined by ρ and ω is perpendicular to this view since ω is orthogonal to \mathcal{R} . The Radon plane contains x since $\rho = \omega \cdot x$ for the evaluation of Eq. (35). Obviously

$$|x| \cos \varepsilon = \omega \cdot x = \rho. \quad (38)$$

We compute the distance r measured from $x/2$ to $\rho\omega$ with the help of the law of cosine:

$$r^2 = \left(\frac{1}{2}|x|\right)^2 + \rho^2 - 2\frac{1}{2}|x|\rho \cos \varepsilon. \quad (39)$$

Exchanging $|x| \cos \varepsilon$ by ρ yields $r = |x|/2$, which is independent of ρ and ω . In other words, the Radon values required in Eq. (35) are located on the surface of a sphere with radius r . The center of this Radon sphere is located at $x/2$ as illustrated in Figure 14.

As discussed previously, a CT scanner measures line integrals, such that Eq. (35) cannot be applied directly. Grangeat (1991) found a relation between the first derivative of the Radon transform and cone-beam projections. Based on this relation, different authors proposed reconstruction algorithms for the helical trajectory, which can also be applied to CT data with projections truncated along z (Kudo, Noo and Defrise, 1998; Schaller *et al.*, 2000; Tam *et al.*, 1999). Nevertheless, reconstruction algorithms based on direct Radon inversion tend to be inefficient and numerically unstable. The theory of Radon inversion will be used in the sequel for the derivation of filtered backprojection (FBP) algorithms. These FBP algorithms are numerically very efficient and yield results in which artefacts result only from the discrete implementation.

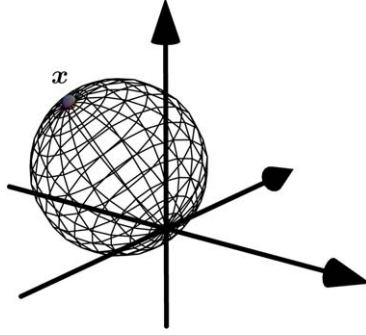


FIGURE 14. Radon values located on the surface of a sphere are required for the evaluation of the inverse Radon transform at \mathbf{x} according to Eq. (35). The center of the Radon sphere is located at $\mathbf{x}/2$ and the radius of the sphere is equal to $|\mathbf{x}/2|$.

2. Fourier Slice Theorem

The Fourier slice theorem gives an important relation between the Radon transform and the object function in the Fourier domain. For its derivation we consider Eq. (34) and perform the Fourier transform along ρ :

$$\begin{aligned}
 \mathcal{FR}\mu(\tilde{\rho}, \omega) &= \int_{-\infty}^{\infty} d\rho \exp(-2\pi i \tilde{\rho} \rho) \mathcal{R}\mu(\rho, \omega) \\
 &= \int_{-\infty}^{\infty} d\rho \exp(-2\pi i \tilde{\rho} \rho) \int_{-\infty}^{\infty} d^3 \mathbf{x} \mu(\mathbf{x}) \delta(\rho - \omega \cdot \mathbf{x}) \\
 &= \int_{-\infty}^{\infty} d^3 \mathbf{x} \mu(\mathbf{x}) \exp(-2\pi i \tilde{\rho} \omega \cdot \mathbf{x}), \tag{40}
 \end{aligned}$$

where in the last step the δ -function was evaluated for the integration over ρ . Now, introducing the 3D Fourier transform of the object function

$$\mathcal{F}\mu(\tilde{x}, \tilde{y}, \tilde{z}) = \int_{-\infty}^{\infty} d^3 \mathbf{x} \exp(-2\pi i (x\tilde{x} + y\tilde{y} + z\tilde{z})) \mu(x, y, z) \tag{41}$$

and using Eq. (36) yields

$$\mathcal{FR}\mu(\tilde{\rho}, \omega) = \mathcal{F}\mu(\tilde{x}, \tilde{y}, \tilde{z}) \Big|_{\substack{\tilde{x}=\tilde{\rho} \cos \alpha \sin \vartheta \\ \tilde{y}=\tilde{\rho} \sin \alpha \sin \vartheta \\ \tilde{z}=\tilde{\rho} \cos \vartheta}} \tag{42}$$

The latter equation is known as the *Fourier slice theorem*. It builds a relationship between the Fourier transform of the object function and the Radon transform.

Consider a Radon plane, which is perpendicular to the z -axis, i.e., $\vartheta = 0$. According to Eq. (42) we have to set $\tilde{x} = \tilde{y} = 0$ for these planes. In other words, planes perpendicular to the z -axis contribute only to vanishing frequency components along xy . Next, consider a Radon plane, that is nearly perpendicular to the z -axis, i.e., ϑ is small. The maximum value of $\tilde{\rho}$ is of the order of the largest frequency necessary to describe the object function (or the Nyquist frequency). Therefore, $\tilde{\rho} \sin \vartheta$ is much smaller than this frequency and \tilde{x} and \tilde{y} are small. In conclusion,

Radon planes, which are nearly perpendicular to the z -axis, contribute to low-frequency components of trans-axial slices only.

B. Exact Filtered Backprojection

Reconstruction algorithms discussed in this chapter share the basic principles. The formulas describing these principles are described in this section before discussion in subsequent sections of how these equations can be applied to different trajectories.

1. Derivative of the Projection Data

The derivative of the projection data is of particular interest. Specifically, we consider the derivative of the line integral data [compare with Eq. (3)] with respect to s :

$$D'(\mathbf{y}(s), \boldsymbol{\theta}) = \left. \frac{\partial D(\mathbf{y}(q), \boldsymbol{\theta})}{\partial q} \right|_{q=s}. \quad (43)$$

Notice that (since $\boldsymbol{\theta}$ is constant) the evaluation of the differentiation requires the consideration of parallel rays from different source positions. Therefore, the differentiation can be computed by considering data along the rows of the wedge detector. Using Fourier filtering techniques, differentiated data along a complete wedge-detector row can be obtained in a single processing step. Furthermore, Fourier techniques allow a modification of the filter in Fourier space. The latter can, for example, be used to suppress the high and emphasize the low frequencies.

On the other hand, the Fourier filtering approach requires two rebinning steps. Data must be rebinned from focus to wedge geometry before filtering

and back to focus geometry afterward. The determination of the derivative via discrete differences is computationally more efficient. A smart way to compute the derivative using discrete differences was published by [Noo, Pack and Heuscher \(2003\)](#).

2. Reconstruction Formula

We assume that the trajectory is described by a vector $\mathbf{y}(s)$ similar to Eqs. (4), (5), or (6). Let us introduce the unit vector $\mathbf{b}(s, \mathbf{x})$ pointing from $\mathbf{y}(s)$ to the object point at \mathbf{x} :

$$\mathbf{b}(s, \mathbf{x}) = \frac{\mathbf{x} - \mathbf{y}(s)}{|\mathbf{x} - \mathbf{y}(s)|}. \quad (44)$$

Furthermore we consider a set of unit vectors $\mathbf{e}_v(s, \mathbf{x})$ and a set of corresponding constants (weights) μ_v , $v = 1, \dots, N_e$. Vectors \mathbf{e}_v and weights μ_v are trajectory-specific (or algorithm specific) reconstruction parameters. They must be chosen properly, as will become evident below.

Generally, the number of \mathbf{e} -vectors, N_e , can depend on s . Each \mathbf{e} -vector is supposed to be orthogonal to $\mathbf{b}(s, \mathbf{x})$, such that each pair $\mathbf{b}(s, \mathbf{x})$ and $\mathbf{e}_v(s, \mathbf{x})$ spans a plane containing \mathbf{x} and \mathbf{y} . We denote these planes as κ -planes. See [Figure 15](#) for an illustration.

We introduce the backprojection interval $I_{BP}(\mathbf{x})$ and the backprojection segment $C_{BP}(\mathbf{x})$. For instance, $I_{BP}(\mathbf{x})$ can correspond to the Pi interval introduced in Section II.D. The backprojection interval defines projections, i.e., s -values, which are taken into account for the reconstruction of $\mu(\mathbf{x})$. Similarly, the backprojection segment is the set of all points along the trajectory associated with $I_{BP}(\mathbf{x})$. Therefore,

$$C_{BP}(\mathbf{x}) = \{\mathbf{y}(s) \mid s \in I_{BP}(\mathbf{x})\}. \quad (45)$$

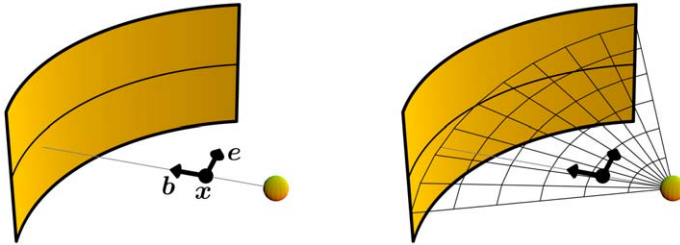


FIGURE 15. Vectors \mathbf{b} and \mathbf{e} span a plane containing the object point \mathbf{x} and the focal spot \mathbf{y} . We denote these planes as κ -planes. κ -Planes must not be confused with Radon planes.

The reconstruction formula derived in this section is

$$\tilde{\mu}(\mathbf{x}) = \frac{-1}{2\pi^2} \int_{I_{\text{BP}}(\mathbf{x})} ds \frac{I(s, \mathbf{x})}{|\mathbf{x} - \mathbf{y}(s)|}, \quad (46)$$

where

$$I(s, \mathbf{x}) = \sum_{v=1}^{N_e} \mu_v \int_{-\pi}^{\pi} \frac{d\gamma}{\sin \gamma} D'(\mathbf{y}(s), \cos \gamma \mathbf{b} + \sin \gamma \mathbf{e}_v) \quad (47)$$

and D' is given by Eq. (43). Eq. (46) corresponds to an exact reconstruction algorithm, if the reconstruction parameters $\mathbf{e}_v(s, \mathbf{x})$ and μ_v have been chosen properly.

For the derivation of Eq. (46), we evaluate Eq. (3) at

$$\boldsymbol{\theta}(\gamma) = \cos \gamma \mathbf{b}(s, \mathbf{x}) + \sin \gamma \mathbf{e}_v(s, \mathbf{x}), \quad (48)$$

where $-\pi \leq \gamma \leq \pi$. Inserting Eq. (35) we obtain

$$\begin{aligned} D(\mathbf{y}, \cos \gamma \mathbf{b} + \sin \gamma \mathbf{e}_v) \\ = \frac{-1}{8\pi^2} \int d\ell \int d\Omega \mathcal{R}'' \mu(\boldsymbol{\omega} \cdot [\mathbf{y} + \ell(\cos \gamma \mathbf{b} + \sin \gamma \mathbf{e}_v)], \boldsymbol{\omega}), \end{aligned} \quad (49)$$

where $d\Omega = d\vartheta \sin \alpha d\alpha$. Eq. (47) becomes

$$\begin{aligned} I(s, \mathbf{x}) &= \frac{-1}{8\pi^2} \sum_{v=1}^{N_e} \mu_v \int \frac{d\gamma}{\sin \gamma} \int d\ell \int d\Omega \\ &\quad \frac{\partial}{\partial q} \mathcal{R}'' \mu(\boldsymbol{\omega} \cdot [\mathbf{y}(q) + \ell(\cos \gamma \mathbf{b} + \sin \gamma \mathbf{e}_v)], \boldsymbol{\omega}) \Big|_{q=s} \end{aligned} \quad (50)$$

by insertion of Eq. (49). Inserting a δ -function

$$\begin{aligned} &\delta(\boldsymbol{\omega} \cdot [\mathbf{y}(q) + \ell(\cos \gamma \mathbf{b} + \sin \gamma \mathbf{e}_v)] - \xi) \\ &= \int_{-\infty}^{\infty} d\rho e^{2\pi i \rho (\boldsymbol{\omega} \cdot [\mathbf{y}(q) + \ell(\cos \gamma \mathbf{b} + \sin \gamma \mathbf{e}_v)] - \xi)} \end{aligned} \quad (51)$$

we make $\mathcal{R}'' \mu$ depend on ξ

$$\begin{aligned} I(s, \mathbf{x}) &= \frac{-1}{8\pi^2} \sum_{v=1}^{N_e} \mu_v \int \frac{d\gamma}{\sin \gamma} \int d\ell \int d\Omega \int d\rho \int d\xi \\ &\quad \frac{\partial}{\partial q} e^{2\pi i \rho (\boldsymbol{\omega} \cdot [\mathbf{y}(q) + \ell(\cos \gamma \mathbf{b} + \sin \gamma \mathbf{e}_v)] - \xi)} \Big|_{q=s} \mathcal{R}'' \mu(\xi, \boldsymbol{\omega}). \end{aligned} \quad (52)$$

Next, we make a change of variables $u_1 = \ell \cos \gamma$, $u_2 = \ell \sin \gamma$, such that

$$\frac{d\ell d\gamma}{\sin \gamma} = \frac{\ell d\ell d\gamma}{u_2} = \frac{du_1 du_2}{u_2}. \quad (53)$$

Using this, the integrations over ℓ and γ yield (Jeffrey, Gradshteyn and Ryzhik, 1994)

$$\begin{aligned} & \int \frac{du_2}{u_2} \int du_1 \exp(2\pi i \rho \boldsymbol{\omega} \cdot (u_1 \mathbf{b} + u_2 \mathbf{e}_v)) \\ &= i\pi \operatorname{sgn}(\rho \boldsymbol{\omega} \cdot \mathbf{e}_v) \delta(\rho \boldsymbol{\omega} \cdot \mathbf{b}) \\ &= i\pi \operatorname{sgn}(\boldsymbol{\omega} \cdot \mathbf{e}_v) \delta(\boldsymbol{\omega} \cdot \mathbf{b}) / \rho \\ &= i\pi |\mathbf{x} - \mathbf{y}(s)| \operatorname{sgn}(\boldsymbol{\omega} \cdot \mathbf{e}_v) \delta(\boldsymbol{\omega} \cdot (\mathbf{x} - \mathbf{y}(s))) / \rho, \end{aligned} \quad (54)$$

where the last step follows directly from Eq. (44). The derivative with respect to q in Eq. (52) yields a factor $2\pi i \rho \boldsymbol{\omega} \cdot \dot{\mathbf{y}}(s)$, and together with Eq. (54) we obtain

$$\begin{aligned} I(s, \mathbf{x}) &= \frac{-1}{8\pi^2} i\pi |\mathbf{x} - \mathbf{y}(s)| \sum_{v=1}^{N_e} \mu_v \int d\Omega \int d\rho \int d\xi \, 2\pi i \rho \boldsymbol{\omega} \cdot \dot{\mathbf{y}}(s) \\ &\quad \operatorname{sgn}(\boldsymbol{\omega} \cdot \mathbf{e}_v) \delta(\boldsymbol{\omega} \cdot (\mathbf{x} - \mathbf{y}(s))) / \rho e^{2\pi i \rho (\boldsymbol{\omega} \cdot \mathbf{y}(s) - \xi)} \mathcal{R}'' \mu(\xi, \boldsymbol{\omega}) \\ &= \frac{1}{4} |\mathbf{x} - \mathbf{y}(s)| \sum_{v=1}^{N_e} \mu_v \int d\Omega \boldsymbol{\omega} \cdot \dot{\mathbf{y}}(s) \operatorname{sgn}(\boldsymbol{\omega} \cdot \mathbf{e}_v) \\ &\quad \delta(\boldsymbol{\omega} \cdot (\mathbf{x} - \mathbf{y}(s))) \mathcal{R}'' \mu(\boldsymbol{\omega} \cdot \mathbf{x}, \boldsymbol{\omega}), \end{aligned} \quad (55)$$

where in the last step the integrations over ρ and ξ were performed. We made $\mathcal{R}'' \mu$ depend on $\boldsymbol{\omega} \cdot \mathbf{x}$ using the δ -function under the integral. For the evaluation of the δ -function, remember that $\boldsymbol{\omega}$ is the normal vector of a Radon plane, which contains the object point \mathbf{x} . Vector $(\mathbf{x} - \mathbf{y}(s))$ points from the focal spot to \mathbf{x} . Therefore, the argument of the δ -function vanishes exactly at those points $\mathbf{y}(s_{\tilde{k}})$, at which the Radon plane intersects with the trajectory. Using the scaling property of the δ -function, we obtain

$$\delta(\boldsymbol{\omega} \cdot (\mathbf{x} - \mathbf{y}(s))) = \sum_{\tilde{k}} \frac{\delta(s - s_{\tilde{k}})}{|\boldsymbol{\omega} \cdot \dot{\mathbf{y}}(s)|}, \quad (56)$$

where the sum runs over *all* intersection points $s_{\tilde{k}}$ of the trajectory with the Radon plane defined by \mathbf{x} and normal vector $\boldsymbol{\omega}$.

The main result of this section is obtained by integration of $I(s, \mathbf{x})$ over s as in Eq. (46). It yields

$$\tilde{\mu}(\mathbf{x}) = \frac{-1}{8\pi^2} \int d\Omega \mathcal{R}'' \mu(\boldsymbol{\omega} \cdot \mathbf{x}, \boldsymbol{\omega}) w(\mathbf{x}, \boldsymbol{\omega}), \quad (57)$$

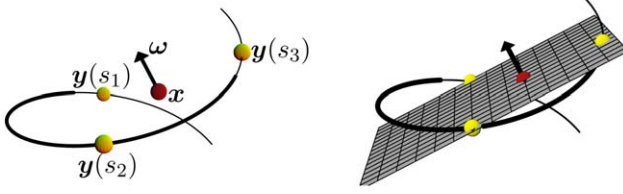


FIGURE 16. The backprojection segment $C_{BP}(\mathbf{x})$ associated with $I_{BP}(\mathbf{x})$ for the object point \mathbf{x} is drawn in bold along the helix. The Radon plane defined by \mathbf{x} and $\boldsymbol{\omega}$ has three intersection points with the helix: $\mathbf{y}(s_1)$, $\mathbf{y}(s_2)$, and $\mathbf{y}(s_3)$. It has only one intersection point, $\mathbf{y}(s_2)$, with $C_{BP}(\mathbf{x})$.

where

$$w(\mathbf{x}, \boldsymbol{\omega}) = \sum_k^{N_I} \sum_{v=1}^{N_e(k)} \mu_v \operatorname{sgn}(\boldsymbol{\omega} \cdot \dot{\mathbf{y}}(s_k)) \operatorname{sgn}(\boldsymbol{\omega} \cdot \mathbf{e}_v). \quad (58)$$

The sum over k is different from the sum over \tilde{k} in Eq. (56). The reason for this is that the integration over s was performed over $I_{BP}(\mathbf{x})$. Therefore, all s_k fulfill $s_k \in I_{BP}(\mathbf{x})$. In other words, k counts all intersection points (IPs) of the Radon plane (associated with $\boldsymbol{\omega}$) with the backprojection segment $C_{BP}(\mathbf{x})$ along the trajectory, whereas \tilde{k} counts all IPs of the Radon plane with the complete trajectory (Figure 16). As mentioned, the number of \mathbf{e}_v -vectors, which we define, can depend on s . Therefore, N_e depends on k in Eq. (58). In the following we denote Radon planes as m -planes, if they have m IPs with $C_{BP}(\mathbf{x})$.

Comparing Eqs. (35) and (57), we realize that Eq. (57) is the inverse Radon transform if and only if $w(\mathbf{x}, \boldsymbol{\omega})$ is identical to one independent of \mathbf{x} and $\boldsymbol{\omega}$. Therefore, if we define all \mathbf{e}_v and μ_v properly, such that this requirement is fulfilled, we derive a reconstruction algorithm that is mathematically exact. Subsequent sections are devoted to adequate definitions of these variables for different cases. First, we describe the general scheme of the reconstruction algorithm and show how it can be implemented efficiently. Section III.C shows how Eq. (58) can be evaluated using projections onto the planar detector.

3. Mathematically Complete Trajectories

The foregoing discussion showed that we want to define the parameters of our reconstruction algorithms in such a way that Eq. (58) results in a constant value of 1. Here we elaborate on the requirements that the trajectory must fulfill. The result is known as the *Tuy condition* (Tuy, 1983).

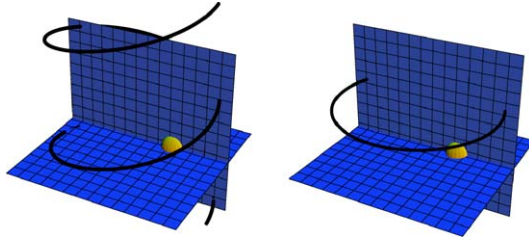


FIGURE 17. Every Radon plane intersects at least once with the helix (left). The circular trajectory is incomplete for object points located outside of the circle plane (right).

Remember that k in Eq. (58) counts the number of IPs of the Radon plane with the backprojection segment $C_{BP}(\mathbf{x})$. Therefore, if Radon planes exist, which do not intersect with $C_{BP}(\mathbf{x})$, Eq. (58) will always give a vanishing result for these planes. In other words, an object point \mathbf{x} is reconstructible only if every Radon plane containing \mathbf{x} intersects with $C_{BP}(\mathbf{x})$ at least once. Trajectories fulfilling this requirement for all \mathbf{x} in the ROI are denoted complete. Figure 17 illustrates completeness and incompleteness using the helical and circular trajectories as examples.

In practice, an even a stronger restriction exists. The argumentation so far neglects the finite size of the detector. Taking the detector dimensions into account, a certain trajectory is complete, if every Radon plane that contains \mathbf{x} has at least one IP from which \mathbf{x} is projected onto the detector. In the sequel, we tacitly assume that $I_{BP}(\mathbf{x})$ is defined such that \mathbf{x} is projected onto the detector from every point within $C_{BP}(\mathbf{x})$. This ensures that a certain trajectory is complete if every Radon plane that contains \mathbf{x} intersects with $C_{BP}(\mathbf{x})$.

4. Reconstruction Algorithm

In the following we assume that vectors \mathbf{e}_v and weights μ_v have been defined such that Eq. (58) results in a constant value of 1. With this assumption, Eqs. (47) and (46) define a reconstruction algorithm, which recovers the μ -values in a mathematically exact way. The reconstruction steps are as follows:

1. Compute the derivative in the sense of Eq. (43).
2. Filter the differentiated data, i.e., filter $D'(y(s), \theta)$.
3. Perform the backprojection along $I_{BP}(\mathbf{x})$ —evaluate Eq. (46).

Steps 1 and 2 follow from Eq. (47): the filtering is performed along γ with kernel $1/\sin \gamma$. The filtering depends on \mathbf{x} only via $\mathbf{b}(s, \mathbf{x})$. Now, all object points on one particular line from the focal spot to the detector share the same \mathbf{b} .

Consider two vectors \mathbf{b}_1 and \mathbf{b}_2 , where \mathbf{b}_2 is located in the κ -plane of \mathbf{b}_1 . In many cases, \mathbf{b}_1 is also located in the κ -plane of \mathbf{b}_2 . Now the filtering step

is shift invariant. Therefore, using Fourier techniques, filtered values for all object points in the κ -plane spanned by \mathbf{b} and \mathbf{e}_ν (see Figure 15) can be obtained in one single processing step. Independent of this observation, this processing step must be repeated for each ν , i.e., the sum over ν must be calculated. The filtering step is further discussed in Section III.B.5.

The backprojection in step 3 corresponds to the integration over s in Eq. (46). It incorporates the sum over ν in Eq. (47) using the weights μ_ν . Section III.B.7 shows how the backprojection can be implemented most efficiently using wedge-detector geometry.

5. Filtering

The filtering, i.e., the integration over γ in Eq. (47), is one of the central steps of the FBP algorithms discussed here. The vectors \mathbf{e}_ν define which data must be involved in the filtering step. In practice, vectors \mathbf{e}_ν are not the most useful quantities for parameterization of the filtering. Instead, we consider the intersection of the κ -planes with the planar detector (Figure 18). The line of intersection defines the filter line, which is sometimes called a κ -line. Any κ -line can be parameterized by two constants, which we denote as v_0 and σ . With these, points on the κ -line are given by

$$v_{\text{PE}}(u_{\text{PE}}) = v_0 + \sigma u_{\text{PE}} \quad (59)$$

in planar-detector coordinates. We derive some relationships between the quantities of a κ -plane and the corresponding κ -line in the following.

Consider the line containing the focal spot at $\mathbf{y}(s)$ and being parallel to $\boldsymbol{\theta}(\gamma)$ defined in Eq. (48). Points on this line are given by

$$\boldsymbol{\ell}(\lambda, \gamma) = \mathbf{y}(s) + \lambda \boldsymbol{\theta}(\gamma), \quad (60)$$

where λ parameterizes the points. Obviously, this line lies in the κ -plane. It intersects with the planar detector, if

$$0 = \boldsymbol{\ell}(\lambda_0, \gamma) \cdot \mathbf{w}(s) = R + \lambda_0 [\cos \gamma \mathbf{b} \cdot \mathbf{w} + \sin \gamma \mathbf{e} \cdot \mathbf{w}], \quad (61)$$

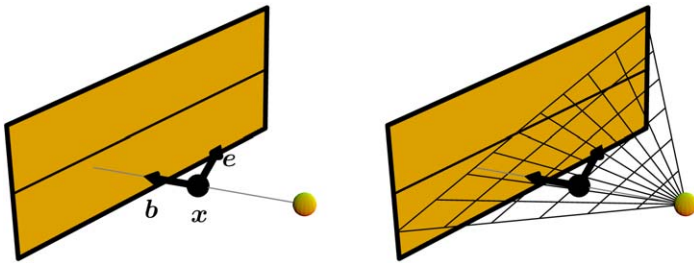


FIGURE 18. The intersection of the κ -plane with the planar detector defines the κ -line.

where $\mathbf{w}(s)$ corresponds to the basis vector defined in Section II.C [see Eq. (15)]. Here, we have used the fact that $\mathbf{y} \cdot \mathbf{w} = R$ for the trajectories considered in this chapter. The point of intersection is parameterized by λ_0 . From the latter equation we derive

$$\lambda_0 = \frac{-R}{\cos \gamma \mathbf{b} \cdot \mathbf{w} + \sin \gamma \mathbf{e} \cdot \mathbf{w}}. \quad (62)$$

With these results points on the κ -line can be parameterized by angle γ as

$$u_{P\ell}(\gamma) = \ell(\lambda_0, \gamma) \cdot \mathbf{u}(s) = -R \frac{\cos \gamma \mathbf{b} \cdot \mathbf{u} + \sin \gamma \mathbf{e} \cdot \mathbf{u}}{\cos \gamma \mathbf{b} \cdot \mathbf{w} + \sin \gamma \mathbf{e} \cdot \mathbf{w}}, \quad (63)$$

$$v_{P\ell}(\gamma) = \ell(\lambda_0, \gamma) \cdot \mathbf{v}(s) - y_z(s) = -R \frac{\cos \gamma \mathbf{b} \cdot \mathbf{v} + \sin \gamma \mathbf{e} \cdot \mathbf{v}}{\cos \gamma \mathbf{b} \cdot \mathbf{w} + \sin \gamma \mathbf{e} \cdot \mathbf{w}}, \quad (64)$$

where we have used $\mathbf{y} \cdot \mathbf{v} - y_z = 0$. Finally, we compute the parameters of Eq. (59). Since σ corresponds to the gradient of the filter line, it can be computed from the last two equations by

$$\sigma = \frac{v_{P\ell}(\gamma_2) - v_{P\ell}(\gamma_1)}{u_{P\ell}(\gamma_2) - u_{P\ell}(\gamma_1)} \quad (65)$$

for arbitrary but different γ_1 and γ_2 . Parameter v_0 corresponds to the $v_{P\ell}$ -coordinate of the κ -line at $u_{P\ell} = 0$. It is given by

$$v_0 = v_{P\ell}(\gamma_0), \quad \tan \gamma_0 = -\frac{\mathbf{b} \cdot \mathbf{u}}{\mathbf{e} \cdot \mathbf{u}}, \quad (66)$$

where γ_0 is defined by the condition $u_{P\ell}(\gamma_0) = 0$.

So far we have considered the case that vectors \mathbf{b} and \mathbf{e} define the filtering plane. Based on this, we have computed the parameters in Eq. (59). For completeness, we now follow the opposite approach: we assume that the κ -line is given by Eq. (59) and compute vectors \mathbf{b} and \mathbf{e} . Since Eq. (14) gives points in world coordinates, vector \mathbf{b} associated with coordinate $u_{P\ell}$ and the filter line under consideration can be computed via

$$\mathbf{b}(u_{P\ell}) = \frac{u_{P\ell} \mathbf{u}(s) + (v_{P\ell}(u_{P\ell}) + y_z(s)) \mathbf{v}(s) - \mathbf{y}(s)}{|u_{P\ell} \mathbf{u}(s) + (v_{P\ell}(u_{P\ell}) + y_z(s)) \mathbf{v}(s) - \mathbf{y}(s)|}. \quad (67)$$

For convenience we introduce vector

$$\mathbf{w}_1(u_{P\ell}) = \mathbf{b}(u_{P\ell} + \Delta u) - \mathbf{b}(u_{P\ell}), \quad (68)$$

which is parallel to the filter line. Since vector \mathbf{e} is parallel to the κ -plane, it is a linear combination of $\mathbf{b}(u_{P\ell})$ and $\mathbf{w}_1(u_{P\ell})$. Furthermore, \mathbf{e} is orthogonal to \mathbf{b} . A vector that fulfills both criteria is given by

$$\mathbf{w}_T(u_{P\ell}) = \mathbf{w}_1(u_{P\ell}) - (\mathbf{w}_1 \cdot \mathbf{b}) \mathbf{b}(u_{P\ell}). \quad (69)$$

Normalization gives

$$e(u_{P\ell}) = \frac{w_T}{|w_T|}. \quad (70)$$

6. Efficient Filtering

So far we have considered reconstruction as computing the μ -value of one particular object point. In practice, reconstruction aims at computing the absorption coefficients in the ROI. Therefore, we now change our paradigm from an object-point-driven reconstruction to a projection-driven reconstruction. For this we assume that we have a set of filter lines distributed over the detector. [Figure 19](#) shows an example. Each of the filter lines shown corresponds to a κ -line in the sense of [Figure 18](#). Each filter line intersects with the $u_{P\ell}$ -axis at a certain v_0 . The gradient in the sense of [Eq. \(59\)](#) is given by

$$\sigma = \frac{v_0}{R} \cot \frac{v_0}{h} \quad (71)$$

for each of the filter lines in our example. The number of filter lines shown in [Figure 19](#) must not be confused with the sum over ν in [Eq. \(47\)](#). The example in [Figure 19](#) has only one set of filter lines: the sum takes only the value $\nu = 1$.

As discussed in further detail in [Section III.E](#) the described filter lines suffice for exact reconstruction using the Pi segment. Within the Pi segment,

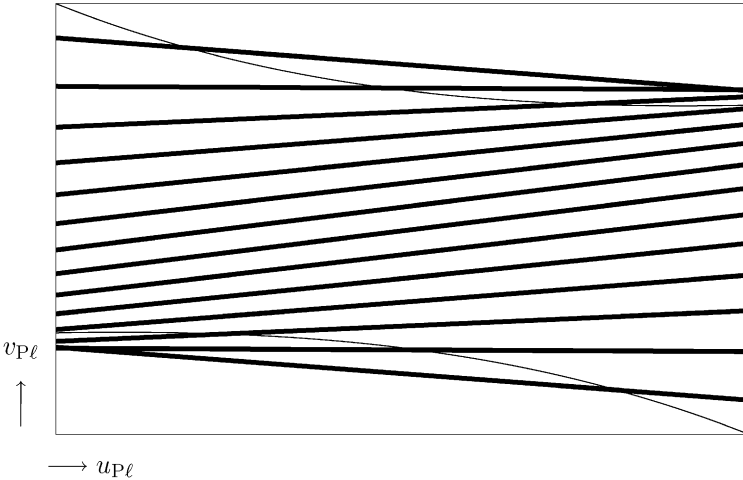


FIGURE 19. The Pi window on the planar detector and filter lines for exact reconstruction along the Pi segment.

any object point will be projected into the Pi window. From each source position it will be projected onto a certain filter line. Now, the filter lines are defined such that the filtered value at the point of projection should be used for the backprojection. With this a projection-driven reconstruction can be phrased as follows:

1. Transform each projection into one or more filtered projections.
2. During the backprojection use the filtered values associated with the points onto which the object point is projected from each source position.

Step 1 indicates that we perform the filtering along each of the filter lines, by which we obtain filtered values along the filter lines. For the backprojection in step 2, we might need to take different sets of filter lines into account and sum these using the correct weights. In other words, we must perform the sum over ν in Eq. (47) and use the weights μ_ν .

Using the results of Section III.B.5 points on the filter lines can be parameterized by angle γ . With this, the filtering along each line can be performed based on Eq. (47); that is, we must perform the integration over γ utilizing the shift invariance of the filtering kernel. In practice, the measured data are associated with the focus detector, whereas the filter lines have been defined on the planar detector. The relationship between focus- and planar-detector variables is given by the formulas in Section II.C. We can proceed from one geometry to the other using interpolations. Nevertheless, it is most convenient if we can sample the data on the filter lines equidistantly in the focus-detector variable φ . Sampling the data equidistantly in φ requires fewer interpolations and therefore results in a better resolution.

Angle γ is different from angle φ (Figure 20). Therefore, sampling points equidistantly in γ on the filter lines requires interpolations along ν_F and along φ . In the following we show how the formula for filtering can be

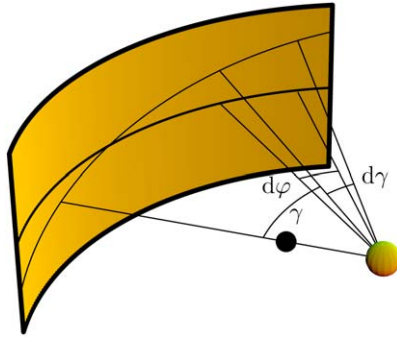


FIGURE 20. Angles γ and φ are measured in different planes.

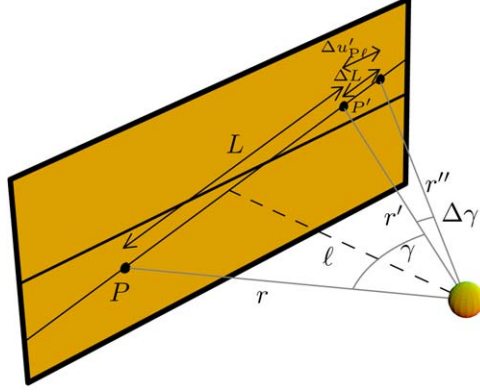


FIGURE 21. The two points $P = (u_{P\ell}, v_{P\ell})$ and $P' = (u'_{P\ell}, v'_{P\ell})$ on the κ -line are separated by angle γ . The dashed line is orthogonal to the κ -line and has length ℓ . The three solid lines originating from the focal spot have lengths r , r' , and r'' .

transformed so that the points on the filter lines can be sampled equidistantly in φ . With the subsequent derivation we follow [Noo, Pack and Heuscher \(2003\)](#) but aim for a slightly different result.

Consider [Figure 21](#). It shows the planar detector and one particular κ -line. Two specific points on the κ -line are denoted as $P = (u_{P\ell}, v_{P\ell})$ and $P' = (u'_{P\ell}, v'_{P\ell})$. They are separated by an angle γ seen from the focal spot. The dashed line is orthogonal to the κ -line and has length ℓ . Using the formulas, which compute the area of a triangle, we observe that $\ell L = r r' \sin \gamma$ and $\ell \Delta L = r' r'' \sin \Delta \gamma$. Hence,

$$\frac{\Delta L}{L} = \frac{r''}{r} \frac{\sin \Delta \gamma}{\sin \gamma}. \quad (72)$$

At the same time $\Delta L/L = \Delta u'_{P\ell} / (u'_{P\ell} - u_{P\ell})$, such that

$$\frac{\Delta u'_{P\ell}}{u'_{P\ell} - u_{P\ell}} = \frac{r''}{r} \frac{\sin \Delta \gamma}{\sin \gamma}. \quad (73)$$

Since we are interested in infinitesimal quantities, this yields

$$\frac{du'_{P\ell}}{u'_{P\ell} - u_{P\ell}} = \frac{r''}{r} \frac{d\gamma}{\sin \gamma}. \quad (74)$$

For the transition to focus-detector coordinates, we realize by comparison with [Eq. \(9\)](#) that

$$u'_{P\ell} - u_{P\ell} = R(\tan \varphi' - \tan \varphi) = R \frac{\sin(\varphi' - \varphi)}{\cos \varphi \cos \varphi'}, \quad (75)$$

such that

$$\frac{du'_{\text{p}\ell}}{d\varphi'} = \frac{R}{\cos^2 \varphi'}. \quad (76)$$

Using this in Eq. (74), we obtain

$$\frac{d\gamma}{\sin \gamma} = \frac{r \cos \varphi}{r' \cos \varphi'} \frac{d\varphi'}{\sin(\varphi' - \varphi)}. \quad (77)$$

The latter equation still contains quantities r and r' . From Figure 21 we can establish

$$\begin{aligned} r^2 \cos^2 \varphi &= (R^2 + u_{\text{p}\ell}^2 + v_{\text{p}\ell}^2) \cos^2 \varphi \\ &= R^2 \left(1 + \tan^2 \varphi + \frac{\tan^2 \lambda}{\cos^2 \varphi} \right) \cos^2 \varphi = \frac{R^2}{\cos^2 \lambda}, \end{aligned} \quad (78)$$

where we have used Eqs. (9) and (10). Now the integration measure can be written as

$$\frac{d\gamma}{\sin \gamma} = \frac{\cos \lambda'}{\cos \lambda} \frac{d\varphi'}{\sin(\varphi' - \varphi)}. \quad (79)$$

Comparing this result with Eq. (47) allows us to write the filtering step as

$$P_v(s, u_{\text{p}\ell}, v_{\text{p}\ell}) = \int_{-\pi}^{\pi} \frac{d\varphi'}{\sin(\varphi' - \varphi)} \cos \lambda' D'(\mathbf{y}(s), u_{\text{p}\ell}(\varphi'), v_{\text{p}\ell}(\varphi')), \quad (80)$$

where

$$v_{\text{p}\ell}(\varphi') = v_{\text{p}\ell}(u_{\text{p}\ell}(\varphi')), \quad (81)$$

$v_{\text{p}\ell}(u_{\text{p}\ell})$ is defined in Eq. (59), and $u_{\text{p}\ell}(\varphi')$ is given by Eq. (9). The factor $1/\cos \lambda$ in Eq. (79) was not used in Eq. (80). It will be taken into account in the backprojection formula below.

Variable φ in Eq. (80) is associated with $u_{\text{p}\ell}$ via Eq. (9). In other words, Eq. (80) parameterizes the filtered values in coordinates of the planar detector. The relationship with focus-detector coordinates can easily be established with the equations in Section II.C. The index v indicates that the formula in Eq. (80) gives filtered values associated with a specific set of filter lines. Within this set the κ -line containing point $(u_{\text{p}\ell}, v_{\text{p}\ell})$ must be used to obtain the desired filtered value.

The integration, i.e., the filtering, is now performed over the angular variable φ' . The filtering kernel is identical to the one in Eq. (47). Therefore

the shift invariance is preserved. Notice the extra factor $\cos \lambda'$ in Eq. (80). According to Eq. (10) this factor depends only on the focus-detector row. Therefore, the factor $\cos \lambda'$ can easily be taken into account by a simple modification of the projection data. This can be done before or after the derivative D' is computed.

With the applied modifications the backprojection [compare with Eq. (46)] can now be written as

$$\mu(\mathbf{x}) = \frac{-1}{2\pi^2} \int_{I_{BP}(\mathbf{x})} \frac{ds}{|\mathbf{x} - \mathbf{y}(s)|} \frac{1}{\cos \lambda} \sum_{v=1}^{N_e} \mu_v P_v(s, u_{p\ell}(\mathbf{x}, s), v_{p\ell}(\mathbf{x}, s)). \quad (82)$$

Here the factor $1/\cos \lambda$ stems from Eq. (79), since it was not absorbed into Eq. (80). This factor corresponds to a postprocessing step after the filtering. Similar to the factor $1/\cos \lambda'$ in Eq. (80), it depends only on the detector position. This factor can therefore be taken into account by an object-point-independent modification of the filtered projection data. Functions $u_{p\ell}(\mathbf{x}, s)$ and $v_{p\ell}(\mathbf{x}, s)$ correspond to the coordinates of the object point \mathbf{x} projected onto the planar detector from $\mathbf{y}(s)$. These coordinates are given by Eqs. (63) and (64) for $\gamma = 0$.

7. Backprojection Using Wedge Detector Geometry

The backprojection formula [Eq. (82)] contains a factor $1/|\mathbf{x} - \mathbf{y}(s)|$. This factor depends on the object point \mathbf{x} and on the focal-spot position $\mathbf{y}(s)$. Due to this factor the backprojection becomes rather inefficient. Here we show how we can eliminate this factor by a transition to parallel (wedge) detector coordinates. For this consider Figure 22. It shows a plane containing \mathbf{x} and parallel to the x - and y -axes. The source path $\mathbf{y}(s)$ is projected into this plane. Variable φ corresponds to the fan angle under which the object point appears from the projected $\mathbf{y}(s)$. While s corresponds to the angular variation of the source position, variable t is the angle under which the source is seen from \mathbf{x} . From Figure 22 we realize that

$$R ds = \frac{L dt}{\cos \varphi}. \quad (83)$$

Here, L is the distance from the projected object point to the projected focal-spot position. This distance is related to λ via

$$\cos \lambda = \frac{L}{|\mathbf{x} - \mathbf{y}(s)|}, \quad (84)$$

such that we derive from Eq. (83)

$$\frac{ds}{|\mathbf{x} - \mathbf{y}(s)|} = \frac{\cos \lambda}{R \cos \varphi} dt. \quad (85)$$

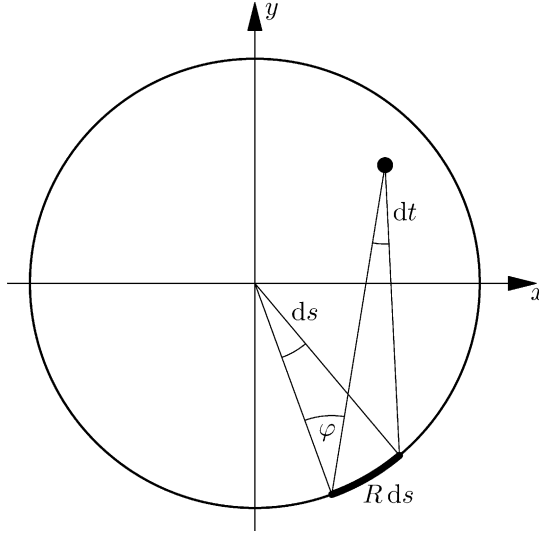


FIGURE 22. Projection of the object point \mathbf{x} into the xy -plane. While angle s is measured from the rotation axis, angle t is measured from the object point.

Using this result, the backprojection formula Eq. (82) becomes

$$\mu(\mathbf{x}) = \frac{-1}{2\pi^2} \int_{\tilde{I}_{BP}(\mathbf{x})} \frac{dt}{R \cos \varphi} \sum_{v=1}^{N_e} \mu_v \tilde{P}_v(t, u_{\parallel}(\mathbf{x}, t), v_{\parallel}(\mathbf{x}, t)). \quad (86)$$

Here, $\tilde{P}_v(t, u_{\parallel}, v_{\parallel})$ corresponds to the filtered projection data rebinned into wedge geometry. Functions $u_{\parallel}(\mathbf{x}, t)$ and $v_{\parallel}(\mathbf{x}, t)$ yield the coordinates of the object point projected onto the wedge detector, and $\tilde{I}_{BP}(\mathbf{x})$ is the backprojection interval of \mathbf{x} in parallel geometry. The factor $1/R \cos \varphi$ in Eq. (86) is independent of the object point \mathbf{x} . This factor varies only with the position on the detector. Again, this factor is taken into account by a modification of the projection data right after filtering.

C. Mathematics on the Planar Detector

The preceding sections describe a certain type of a filtered backprojection algorithm. So far, the algorithm has been presented in its most general way. The subsequent sections are devoted to specific trajectories and acquisition types. The concept of projecting the trajectory and the vectors involved onto

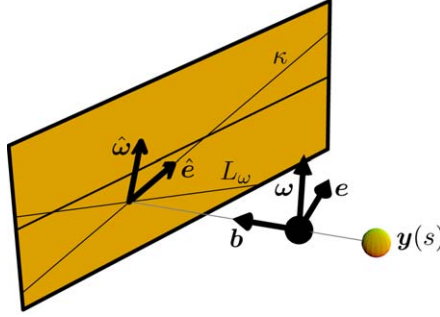


FIGURE 23. The intersection of the κ -plane defined by e and the planar detector results in the shown κ -line. The Radon plane defined by ω intersects with the detector, resulting in line L_ω . Projecting e onto the detector gives vector \hat{e} , which is parallel to the κ -line. The projection of ω , denoted as $\hat{\omega}$, is orthogonal to L_ω .

the planar detector proves very useful (Katsevich, 2004b). Some general formulas helpful for the mathematical discussions that follow are presented here.

The projections of different trajectories were discussed in Section II.D. Now we consider vectors e , ω , and \dot{y} . Remember that vectors e and ω define κ - and Radon planes, respectively. Notice that $\dot{y}(s)$, i.e., the tangent on the trajectory, is parallel to the planar detector for the trajectories considered. Figure 23 shows exemplary vectors e and ω . The projections of these vectors onto the planar detector are denoted as \hat{e} and $\hat{\omega}$. In particular, the κ -line is parallel to \hat{e} , while $\hat{\omega}$ is orthogonal to L_ω . Here, L_ω is the line that results from the intersection of the Radon plane with the detector. Explicit expressions for \hat{e} and $\hat{\omega}$ can be obtained via

$$\hat{e} = (e \times b) \times w \quad (87)$$

and

$$\hat{\omega} = (\omega \times w) \times w = \omega + w(\omega \cdot w). \quad (88)$$

Here, w is the basis vector defined in Section II.C and b is defined in Eq. (44). Furthermore, we used the relation $a \times (b \times c) = b(a \cdot c) - c(a \cdot b)$ above. Now, using the general formula

$$(a \times b) \cdot (c \times d) = (a \cdot c)(b \cdot d) - (b \cdot c)(a \cdot d) \quad (89)$$

twice and applying $b \cdot \omega = 0$, we derive

$$\hat{e} \cdot \hat{\omega} = (w \times \omega) \cdot (e \times b) = -(b \cdot w)(e \cdot \omega). \quad (90)$$

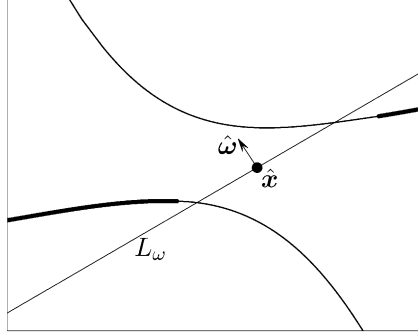


FIGURE 24. The planar detector seen from $y(s_2)$ in Figure 16. The intersection of the Radon plane results in line L_ω . Object point x is projected onto point \hat{x} . The backprojection segment is drawn bold.

Similarly, using $w \cdot \dot{y} = 0$, we obtain from Eq. (88)

$$\hat{\omega} \cdot \dot{y}(s) = \omega \cdot \dot{y}(s). \quad (91)$$

Considering Eqs. (90) and (91) and keeping Eq. (58) in mind yields

$$\text{sgn}(\omega \cdot e) = \text{sgn}(\hat{\omega} \cdot \hat{e}) \quad \text{and} \quad \text{sgn}(\omega \cdot \dot{y}) = \text{sgn}(\hat{\omega} \cdot \dot{y}), \quad (92)$$

where we have used $b \cdot w < 0$.

Comparing Eqs. (58) and (92) shows that for the evaluation of Eq. (58) it is sufficient to consider the projections of the involved vectors onto the planar detector. We further argue that projections onto the planar detector also are useful for answering certain questions (such as, how often does a certain Radon plane intersect with the trajectory?). For an illustration consider Figure 24. It shows the planar detector seen from $y(s_2)$ in Figure 16. The backprojection segment along the helix is drawn bold. As seen, the other two IPs of the Radon plane (besides $y(s_2)$) do not intersect with the backprojection segment.

Eq. (58) is invariant under $\omega \rightarrow -\omega$. We will use this by ensuring that $\text{sgn}(\omega \cdot \dot{y}) = 1$ in the examples given throughout this chapter.

D. Circle Plus Line

This section is devoted to a trajectory consisting of a circle and a line, where the line is parallel to the z -axis. The circle and line trajectory (CLT) is best suited to demonstrate the methods used in this chapter. It is relatively easy to understand, while it requires applications to the typical case differentiations. The resulting reconstruction algorithm was first published by Katsevich (2004a).

1. Geometrical Properties

The parameterization of the trajectory under consideration is shown by Eqs. (4) and (6). The circle and the line intersect at one point, denoted as P_{cl} . For every object point \mathbf{x} a line can be found that contains \mathbf{x} and intersects with the circle and the line. Figure 25 illustrates this concept. In analogy to helical CT, such a line is called a Pi-line. Furthermore, the IPs of the Pi-line with the circle and the line are denoted as $P_{\pi c}$ and $P_{\pi \ell}$, respectively.

Now, we choose the backprojection segment $C_{BP}(\mathbf{x})$ for the CLT to extend from $P_{\pi c}$ to P_{cl} along the circle and from P_{cl} to $P_{\pi \ell}$ along the line. This gives two possibilities along the circle (Figure 25). Using one of these backprojection segments, the combination of the Pi-line and $C_{BP}(\mathbf{x})$ gives a closed contour. Therefore, every Radon plane containing \mathbf{x} intersects with $C_{BP}(\mathbf{x})$ and the trajectory is complete. Moreover, every Radon plane has either one or three IPs with $C_{BP}(\mathbf{x})$. We neglect planes that are tangential on the circle or contain the line since these have a Lebesgue measure zero. As mentioned in Section III.B.2, Radon planes with one IP are denoted as 1-planes, while Radon planes with three IPs are called 3-planes. Radon planes with three IPs intersect twice with the circle and once with the line, whereas 1-planes either have one IP with the line or one IP with the backprojection segment along the circle. Figure 26 illustrates the three different cases.

In the sequel we define filter lines separately for the circle and for the line part of $C_{BP}(\mathbf{x})$. Based on Eq. (58) we show that the filter lines are defined such that every 1-plane receives a weight of 1 from the single IP. Every 3-plane gets a weight of 1 from each of the two IP along the circle. It gets a weight of -1 from the IP on the line, such that the sum over all three weights results in $+1$, as desired.

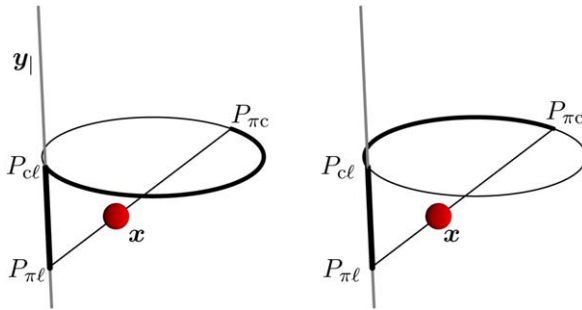


FIGURE 25. The circle and the line intersect at point P_{cl} . For each object point \mathbf{x} a unique Pi-line can be found, which contains \mathbf{x} and intersects with the circle and the line. The points of intersection are denoted as $P_{\pi c}$ and $P_{\pi \ell}$, respectively. For the backprojection segment, which is drawn in bold, the two possibilities are shown in the left and right images.

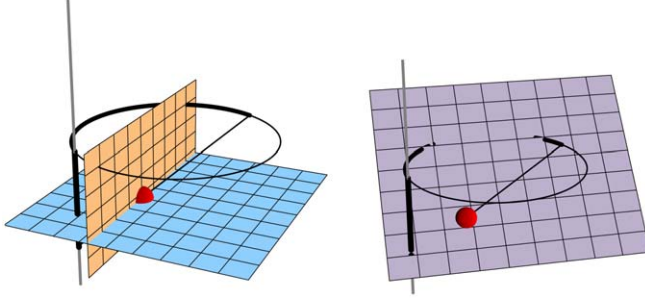


FIGURE 26. Left: The two Radon planes each have one IP with the backprojection segment. Right: The Radon plane has three IPs. For the other possibility of $C_{BP}(\mathbf{x})$, this plane corresponds to a 1-plane.

2. Filter Lines

The methods introduced in Section III.B can be used to parameterize each filter line using planar-detector coordinates. In particular, we specify pairs of constants v_0 and σ , which define a filter line in the sense of Eq. (59). For the circle part of $C_{BP}(\mathbf{x})$, the filter lines used are all parallel to the $u_{P\ell}$ -axis, such that $\sigma = 0$. In other words, specifying a complete set of filter lines for the circle part, parameter v_0 differentiates between different lines of this set. We need to define only one set of filter lines for the circle, such that $N_e = 1$ [compare with Eqs. (47), (58), and (86)]. Moreover, the weights belonging to this filter-line set must be set to $\mu_v = 1$. Figure 27 depicts the filter lines.

We also need one set of filter lines for the line part of the CLT, i.e., $N_e = 1$. The filter lines are tangents on the projected circle. The projection of the circle can be computed with Eq. (22), where $|z_0 - z_1|$ is the distance between the

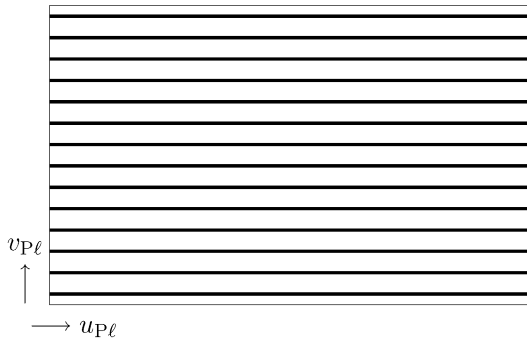


FIGURE 27. The filter lines for the circle part of the CLT are all parallel to the $u_{P\ell}$ -axis.

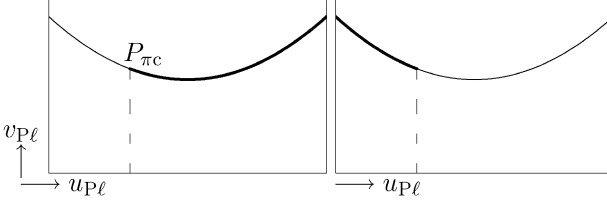


FIGURE 28. Projection of the circle onto the planar detector from a point on the line for the two cases shown in Figure 25. The backprojection segment is drawn bold. The dashed line is the projection of the Pi-line. This projection is parallel to the $v_{P\ell}$ -axis.

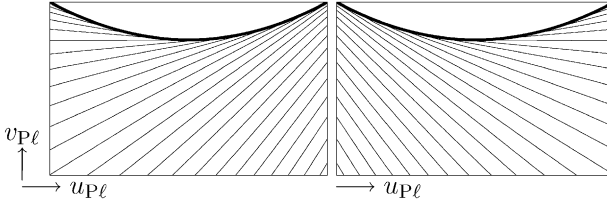


FIGURE 29. Sets of filter lines for a particular point on the line for the two cases shown in Figure 25.

point on the line and the circle plane. Since Eq. (22) depends on z , the sets of filter lines vary for different positions on the line. Figure 28 considers the two different cases for the choice of $C_{BP}(\mathbf{x})$. The backprojection segment is drawn bold, and the projection of the Pi-line is dashed. The specific definition of the filter lines requires that each filter line is tangential on the projected backprojection segment, i.e., on the segments drawn bold in Figure 28. This results in the filter-line sets depicted in Figure 29 for the two cases. Obviously, these filter lines are tangential on the projected circle, and the point of tangency is either right or left of the point onto which \mathbf{x} is projected. The weights must be set such that $\mu_v = 1$ for the case shown in the left image of Figure 29, while $\mu_v = -1$ for the case shown in the right image of Figure 29.

a. Circular Full Scan. For the two possibilities of $C_{BP}(\mathbf{x})$ shown in Figure 25, the two segments on the circle together cover the complete circle. This provides an easy “recipe” for defining a full-scan algorithm, which uses data from the complete circle. We could apply just the algorithm defined above for both cases and average the results. More efficiently, we obtain the same output by performing the backprojection over the complete circle using the filter lines defined above. For the line, we filter the data using both sets of filter lines and add the data before backprojection. In other words, we need to

set $N_e = 2$ in Eqs. (82) and (86). Weights μ_v must be multiplied by $1/2$ for the line part.

3. Proof of Exactness

We now prove that the reconstruction algorithm is mathematically exact. As discussed in Section III.B, we need to show that Eq. (58) results in a constant value of 1 using the defined filter lines and weights. The result of Eq. (58) must be equal to 1 for every object point in the FOV and for every Radon plane containing the object point.

We begin with analyzing the filter lines of the circle part. Remember that every Radon plane either has zero, one or two IPs with the circle part of $C_{BP}(\mathbf{x})$. If it has two IPs, the Radon plane is a 3-plane, i.e., it has one additional IP with the line. According to Section III.C it is sufficient to consider the projection of vectors $\boldsymbol{\omega}$ and \mathbf{e} onto the planar detector. The projected vectors are denoted as $\hat{\boldsymbol{\omega}}$ and $\hat{\mathbf{e}}$, respectively. Moreover, the tangent on the trajectory $\dot{\mathbf{y}}(s)$ is parallel to the planar detector. We defined the filter lines for the circle part to be parallel to the $u_{p\ell}$ -axis. Therefore, $\hat{\mathbf{e}}$ is also parallel to this axis for each filter line. Realizing that $\dot{\mathbf{y}}_o(s)$ is also parallel to the $u_{p\ell}$ -axis, we conclude that the two sgn-functions in Eq. (58) result in $\text{sgn}(\hat{\boldsymbol{\omega}} \cdot \dot{\mathbf{y}}) \text{sgn}(\hat{\boldsymbol{\omega}} \cdot \hat{\mathbf{e}}_v) = \text{sgn}^2(\hat{\boldsymbol{\omega}} \cdot \hat{\mathbf{e}}_v) = 1$. Now, $\mu_v = 1$, $N_e = 1$, and k counts the number of IPs. Therefore, evaluating Eq. (58) only for the circle part results in a value of 0, 1, or 2. In other words, for a 1-plane with IP along the circle, Eq. (58) gives the desired result of 1. For a 3-plane the two IP along the circle contribute with a weight of 2. In the following we therefore must show that the line contributes with a weight of -1 for 3-planes, while 1-planes with IP on the line get a weight of 1.

For the discussion of the filter lines used along the line consider Figure 30. It corresponds to the left image in Figure 28. We assume that the object point under consideration is projected onto point $\hat{\mathbf{x}}$. Remember that \mathbf{x} is located on the Pi-line, which is drawn as a dashed line. The corresponding filter line, which is parallel to vector $\hat{\mathbf{e}}$, is tangential on the projected circle, with the point of tangency located right of $\hat{\mathbf{x}}$. The tangent on the trajectory, $\dot{\mathbf{y}}_l$, is parallel to the $v_{p\ell}$ -axis, i.e., it is parallel to the z -axis. The two dotted lines correspond to exemplary Radon planes with normal vectors $\boldsymbol{\omega}_1$ and $\boldsymbol{\omega}_2$. Obviously the Radon plane associated with $\boldsymbol{\omega}_1$ is a 1-plane. The sole IP is the current source position. The Radon plane associated with $\boldsymbol{\omega}_2$ is a 3-plane, for which only one IP on the circle is shown in Figure 30. The second IP is located farther to the right.

As discussed in Section III.C, Eq. (58) is invariant under $\boldsymbol{\omega} \rightarrow -\boldsymbol{\omega}$. For convenience, we ensure that $\text{sgn}(\boldsymbol{\omega} \cdot \dot{\mathbf{y}}) = 1$ in our examples. The angle between $\hat{\mathbf{e}}$ and $\hat{\boldsymbol{\omega}}_1$ is less than $\pi/2$. Therefore, $\text{sgn}(\hat{\boldsymbol{\omega}}_1 \cdot \hat{\mathbf{e}}) = 1$. Evaluating

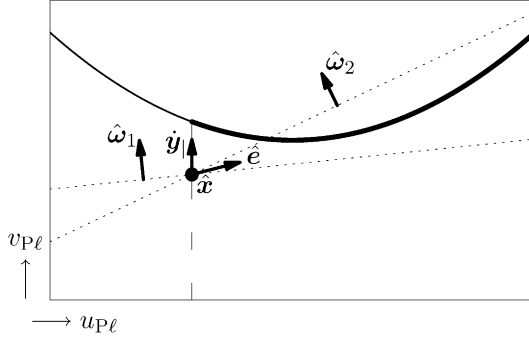


FIGURE 30. The planar detector seen from one point on the line. The two dotted lines correspond to Radon planes with normal vectors ω_1 and ω_2 . The object point is projected onto point \hat{x} . The filter line, which is parallel to \hat{e} , is tangential on the projected circle with the point of tangency located to the right of \hat{x} .

Eq. (58) with $N_e = N_I = 1$ and $\mu_v = 1$, we realize that the Radon plane associated with ω_1 receives a weight of 1, as desired for a 1-plane. The angle between \hat{e} and $\hat{\omega}_2$ is larger than $\pi/2$, such that $\text{sgn}(\hat{\omega}_2 \cdot \hat{e}) = -1$. Now, with $N_I = 3$ we can evaluate Eq. (58) and obtain $1 + 1 - 1 = 1$, where the first two summands stem from the two IPs on the circle. In other words, the 3-plane associated with ω_2 derives the desired weight of 1 from the complete CLT.

Figure 31 shows the situation of Figure 30 for the second possibility of $C_{BP}(\mathbf{x})$. Both Radon planes now correspond to 1-planes. The filter line is tangential on the circle with point of tangency located left of \hat{x} . Obviously,

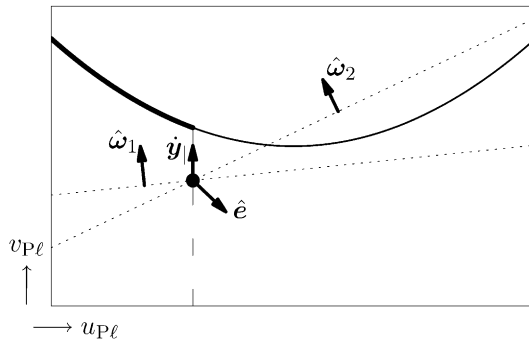


FIGURE 31. The same scenario as in Figure 30 but now for the second case shown in Figure 25. The filter line, which is parallel to \hat{e} , is tangential on the projected circle with point of tangency located left of \hat{x} .

$\text{sgn}(\hat{\omega}_1 \cdot \hat{e}) = \text{sgn}(\hat{\omega}_2 \cdot \hat{e}) = -1$, and with $\mu_v = -1$ Eq. (58) results in a value 1 for the two Radon planes shown.

All Radon planes that can be covered from the current focal spot position $y_l(z)$ must contain $y_l(z)$ and x . Therefore, all these Radon planes can be considered by rotating one of the dashed lines in Figure 30 around \hat{x} . Starting with the line indicated by $\hat{\omega}_1$ and rotating counterclockwise, the associated Radon plane becomes a 3-plane as soon as the line intersects with the circle. Now, since the filter line is tangential on the circle, $\hat{\omega} \cdot \hat{e}$ changes sign exactly at the transition from a 1-plane to a 3-plane. The next sign change occurs when the dashed line becomes parallel to the $v_{p\ell}$ -axis—remember that we want $\text{sgn}(\hat{\omega} \cdot \hat{y}) = 1$. Therefore, we must change $\hat{\omega}$ from pointing to the left to pointing to the right, once the dashed line becomes parallel to $v_{p\ell}$. Again, the sign change occurs exactly at the transition from a 3-plane to a 1-plane, since the projected Pi-line is parallel to the $v_{p\ell}$ -axis. Continuing with the rotation until the dashed line becomes parallel to the line with which we started, no further sign change occurs. In other words, for the current source position and object point x , all Radon planes can be treated in the same way as above for the exemplary Radon planes with normal vectors ω_1 and ω_2 .

The discussion so far has not been specific in the choice of the focal spot position or the object point. Choosing different x and/or $y_l(z)$ all arguments can be repeated. In other words, 1- and 3-planes get the desired weights from all source positions, such that the proof is finished.

4. Reconstruction Results

For the evaluation of the CLT reconstruction algorithm we simulated a CT scanner with 256 detector rows. Table 1 summarizes the simulation parameters of the circle part. The circle plane was located at a distance

TABLE 1
SIMULATION PARAMETERS

Projections per turn	1160	
Detector columns	512	
Detector rows	256	
Fan angle	26.5	degrees
Detector height	291.9	mm
Focal-spot size	0.91×1.37	mm^2
Distance source-rotation axis	570	mm
Distance source-detector center	1040	mm
Detector oversampling	3×3	
Focal-spot oversampling	3×3	
Angular oversampling	3	
Reconstructed voxel size	$(0.5)^3$	mm^3

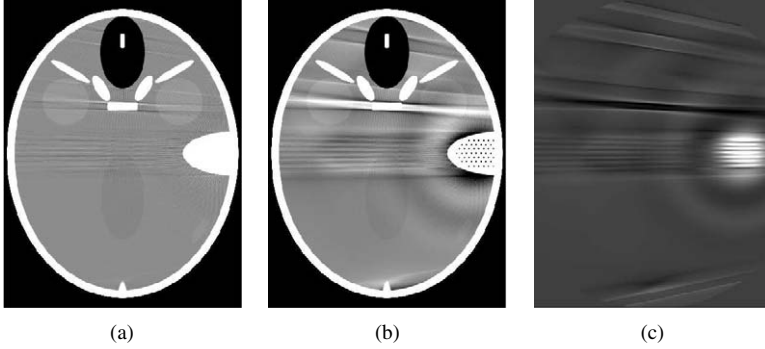


FIGURE 32. Reconstruction results for the CLT. The three images show (a) the result of the complete CLT, (b) the contribution of the circle, and (c) the contribution of the line, respectively. L/W: 40 HU/200 HU for the first two images, L/W: -950 HU/200 HU for the line image. L, level; W, window.

$\Delta z = 40$ mm from the origin of the phantom. For the line part, we simulated 1025 projections over a distance of 320 mm along z . We used the Forbild head phantom (www.imp.uni-erlangen.de/forbild/english/results/head/head.html), which contains some high-frequency components as well as some low-contrast parts. The head phantom therefore is a challenge for every reconstruction algorithm.

Throughout this chapter we use Hounsfield² units (HU) for the presentation of reconstruction results. *Hounsfield units* correspond to a shift and scaling of the absorption coefficients, such that

$$\text{HU}(\mu) = 1000 \frac{\mu - \mu_{\text{H}_2\text{O}}}{\mu_{\text{H}_2\text{O}}}. \quad (93)$$

Here, $\mu_{\text{H}_2\text{O}}$ corresponds to the absorption coefficient of water. We have set $\mu_{\text{H}_2\text{O}} = 0.0183/\text{mm}$. Notice that the shift used in the transition from μ -values to HU must be taken into account when adding images.

Figure 32 shows some reconstruction results. The specification of the level and window (L/W) 40 HU/200 HU means that the available gray-level range is assigned to object points between -60 HU and 140 HU. Object points below -60 HU are drawn as black, while object points above 140 HU are white. Figure 32 shows the result for the complete CLT, as well as the contributions of the circle and the line. The (transaxial) slice shown is perpendicular to the z -axis and has a distance of 45 mm to the circle plane. Obviously, the addition of the line significantly reduces the artefacts visible in the image of the pure circle.

² Sir Godfrey Newbold Hounsfield, English electrical engineer, 1919–2004.

E. The Katsevich Algorithm for Helical Pi Acquisition

The reconstruction algorithms described next deal with helical CT, beginning with the Pi mode. An exact shift invariant FBP algorithm for a helical Pi acquisition was first found by Katsevich (2002). The following sections describe the further improvement of the algorithm published in Katsevich (2004b).

1. Geometrical Properties

The helical trajectory is parameterized by Eq. (5). As discussed in Section II.D, a Pi-line can be found for every object point \mathbf{x} in the FOV. A Pi-line contains \mathbf{x} and two points $\mathbf{y}_H(s_{\pi 1})$, $\mathbf{y}_H(s_{\pi 2})$ on the helix with $s_{\pi 2} - s_{\pi 1} < 2\pi$. All points $\mathbf{y}_H(s)$ on the helix with $s_{\pi 1} \leq s \leq s_{\pi 2}$ belong to the Pi segment of \mathbf{x} . The lower and upper Pi-window boundaries are given by Eq. (32) setting $n = 1$. From every point $\mathbf{y}_H(s)$ within the Pi segment, \mathbf{x} is projected onto the planar detector between these boundaries. For the reconstruction algorithm discussed here, the Pi segment corresponds to the backprojection segment $C_{BP}(\mathbf{x})$.

Since the combination of the Pi-line and the Pi segment gives a closed contour, every Radon plane containing \mathbf{x} intersects with the Pi segment. The trajectory is complete. In particular, every Radon plane has either one or three IPs with $C_{BP}(\mathbf{x})$ (again we neglect planes tangential on the helix, since these have a measure zero). Figure 33 depicts one particular object point \mathbf{x} and its Pi-line. The shown Radon plane intersects three times with the Pi segment, and the IPs are $\mathbf{y}_H(s_1)$, $\mathbf{y}_H(s_2)$, and $\mathbf{y}_H(s_3)$. Figure 34 shows the planar detector seen from the three points $\mathbf{y}_H(s_1)$ through $\mathbf{y}_H(s_3)$. The object point is projected onto different positions indicated by $\hat{\mathbf{x}}$. The dotted lines in Figure 34 correspond to the intersections of the Radon plane with the detector.

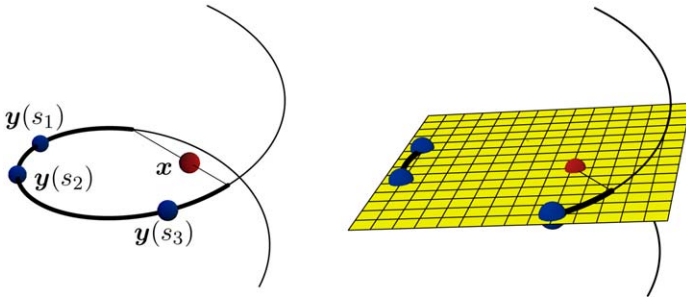


FIGURE 33. The three IPs of the Radon plane are located within the Pi segment of object point \mathbf{x} .

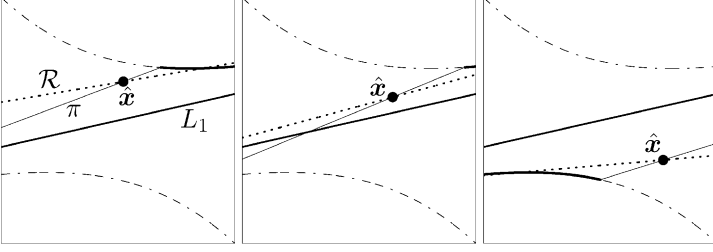


FIGURE 34. The planar detector seen from the three IPs $y_H(s_1)$ through $y_H(s_3)$ in Figure 33. The object point is projected onto points \hat{x} . The dotted lines indicated by \mathcal{R} correspond to the intersections of the Radon plane. Projections of the Pi-line result in the solid lines indicated by π . The other solid line L_1 corresponds to the asymptote on the helix.

The asymptote on the projected helix plays a crucial role. The asymptote is indicated by the solid line L_1 in Figure 34. It is parallel to $\dot{y}_H(s)$. Line L_1 contains the origin of the planar detector and its gradient is equal to \hbar/R . The latter follows from Eq. (32) using $\arctan x \rightarrow (\pi/2 - 1/x)$ for $x \rightarrow \infty$.

The solid lines indicated by π in Figure 34 are the projections of the Pi-line. Remember that the points on the Pi-window boundaries are associated with points on the helix. Traversing these boundaries from right to left the corresponding s -value increases. In particular, two points on the lower and upper Pi-window boundaries at the same u_{Pl} -coordinate are separated by an angular distance of 2π [compare with Eq. (28)]. Since the points of sunrise and sunset now are separated by less than 2π , the Pi-line projected onto the planar detector must have positive slope.

Point $y_H(s_1)$ is the first IP of the exemplary Radon plane in Figure 33, which is reached when traversing the helix. Seen from that point (the first image in Figure 34), the projection of the Radon plane (dotted line) has two IPs with the upper Pi-window boundary. Moreover, these two IPs belong to the Pi segment, since the intersection of the Pi-line with the Pi-window boundary is farther to the left. In summary, from the first image in Figure 34 it can be deduced that the indicated Radon plane is a 3-plane with two further IPs in the future. Similarly, in the second image of Figure 34 the dotted line has a gradient larger than the gradient of L_1 . Therefore, the dotted line has one IP with the lower Pi-window boundary and one IP with the upper one. This indicates that the current source position corresponds to the central IP of the 3-plane.

2. Filter Lines

As discussed in Section III.B, the filtering can be defined using κ -planes or κ -lines, where the latter are the intersection of the κ -planes with the

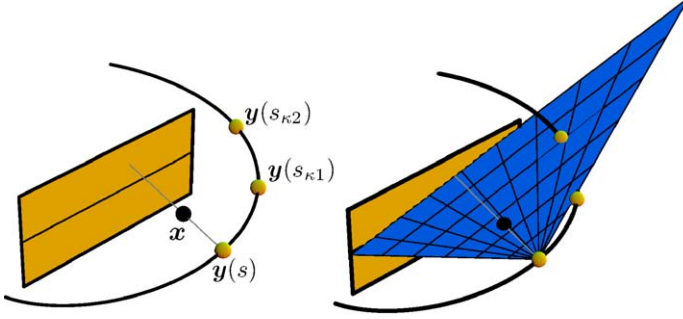


FIGURE 35. The κ -planes used for Pi reconstruction contain the object point \mathbf{x} , the current source position $\mathbf{y}(s)$, and two further points on the helix: $\mathbf{y}(s_{\kappa1})$ and $\mathbf{y}(s_{\kappa2})$. The angular distance $s_{\kappa2} - s$ is twice as large as the distance $s_{\kappa1} - s$.

planar detector. For the reconstruction algorithm described here, the κ -planes correspond to planes that contain the object point, the current source position, and two additional points on the helix denoted as $\mathbf{y}_H(s_{\kappa1})$ and $\mathbf{y}_H(s_{\kappa2})$ in the following. Both points $\mathbf{y}_H(s_{\kappa1})$ and $\mathbf{y}_H(s_{\kappa2})$ must belong to the Pi segment of \mathbf{x} , and they must fulfill $s_{\kappa2} - s_{\kappa1} = s_{\kappa1} - s$, where $\mathbf{y}_H(s)$ corresponds to the current source position (Figure 35). If \mathbf{x} is projected above line L_1 (compare with Figure 34), $s < s_{\kappa1} < s_{\kappa2}$, while $s_{\kappa2} < s_{\kappa1} < s$, if \mathbf{x} is projected below L_1 . If \mathbf{x} is projected onto the asymptote L_1 , the κ -line is identical to L_1 , i.e., the κ -plane is parallel to the tangent on the helix. For the method specified here, the weights must be set to $\mu_v = 1$. We show in the following that the definition of the κ -planes results in filter lines with gradients given by Eq. (71).

For symmetry reasons we can choose the source to be located at $\mathbf{y}_H(0)$. We consider the κ -plane, which contains the focal spot and points $\mathbf{y}_H(s)$ and $\mathbf{y}_H(2s)$. A parameterization of this plane is given by

$$\begin{aligned} \mathbf{p}(\alpha, \beta) &= \mathbf{y}_H(0) + \alpha(\mathbf{y}_H(s) - \mathbf{y}_H(0)) + \beta(\mathbf{y}_H(2s) - \mathbf{y}_H(0)) \\ &= \begin{pmatrix} R \\ 0 \\ 0 \end{pmatrix} + \alpha \begin{pmatrix} R(\cos s - 1) \\ R \sin s \\ \hbar s \end{pmatrix} + \beta \begin{pmatrix} R(\cos 2s - 1) \\ R \sin 2s \\ 2\hbar s \end{pmatrix}. \end{aligned} \quad (94)$$

Due to our choice of parameters the plane intersects with the planar detector at $x = 0$, such that

$$0 = 1 + \alpha(\cos s - 1) + \beta(\cos 2s - 1) \quad (95)$$

gives the condition for the points of intersection. Solving the latter equation for β results in

$$\beta = \frac{1 + \alpha(\cos s - 1)}{1 - \cos 2s} = \frac{1 + \alpha(\cos s - 1)}{2 \sin^2 s}. \quad (96)$$

Inserting this equation into Eq. (94), the y -component corresponds to the u_{Pl} -coordinate of the filter line:

$$\begin{aligned} u_{\text{Pl}}(\alpha) &= R \frac{\sin 2s}{2 \sin^2 s} + \alpha R \left(\sin s + \frac{\sin 2s(\cos s - 1)}{2 \sin^2 s} \right) \\ &= R \cot s + \alpha R \frac{(1 - \cos s)}{\sin s}, \end{aligned} \quad (97)$$

or

$$\alpha(u_{\text{Pl}}) = \frac{u_{\text{Pl}} - R \cot s}{R(1 - \cos s)} \sin s = \frac{u_{\text{Pl}} \sin s - R \cos s}{R(1 - \cos s)}. \quad (98)$$

Similarly, for the parameterization of the v_{Pl} -coordinate of the κ -line, we obtain

$$\begin{aligned} v_{\text{Pl}}(\alpha) &= \frac{\hbar s}{\sin^2 s} + \alpha \hbar s \left(1 + \frac{\cos s - 1}{\sin^2 s} \right) \\ &= \frac{\hbar s}{\sin^2 s} + \alpha \hbar s \frac{\cos s(1 - \cos s)}{\sin^2 s}. \end{aligned} \quad (99)$$

Inserting Eq. (98) gives

$$\begin{aligned} v_{\text{Pl}}(u_{\text{Pl}}) &= \frac{\hbar s}{\sin^2 s} - \hbar s \frac{\cos^2 s}{\sin^2 s} + u_{\text{Pl}} \frac{\hbar s}{R} \frac{\cos s}{\sin s} \\ &= \hbar s + u_{\text{Pl}} \frac{\hbar s}{R} \cot s \\ &= v_0 + u_{\text{Pl}} \frac{v_0}{R} \cot \frac{v_0}{\hbar}, \end{aligned} \quad (100)$$

which is the parameterization of the filter line in the sense of Eqs. (59) and (71) with $v_0 = \hbar s$.

Considering Figure 19 we observe that the defined filter lines cover the complete Pi window, such that a filter line can be found for every object point and for every source position within $C_{\text{BP}}(\mathbf{x})$. Nevertheless, the filter lines have different gradients, such that intersection points exist. For illustration consider Figure 36. The two κ -lines intersect at point P_1 . The definition given above specifies that κ -planes must have three IPs with the Pi segment. Line κ_1 has two IPs outside the Pi segment for object points projected onto P_1 . Remember that the projection of the Pi-line has a positive slope on the planar detector (compare with Figure 34). Therefore, we must use filtered values associated

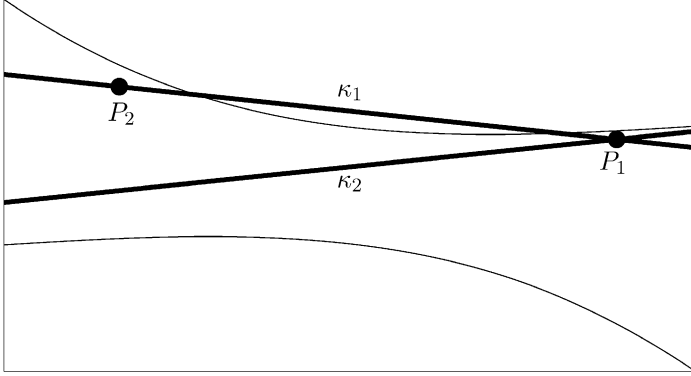


FIGURE 36. The two filter lines κ_1 and κ_2 intersect at point P_1 . For line κ_2 only the corresponding κ -plane has intersection points within the Pi segment of object points projected onto P_1 .

with line κ_2 for points projected onto P_1 . Line κ_1 serves as a filter line for object points projected, for example, onto point P_2 .

3. Proof of Exactness

We now prove that the defined filter lines specify an exact reconstruction algorithm by showing that Eq. (58) results in a constant value of 1. Consider Figure 37. An exemplary object point is projected onto point \hat{x} of the planar detector. The corresponding Pi-line is indicated by π . The line indicated by T contains \hat{x} and is tangential on the upper Pi-window boundary. The Pi-line and line T divide the detector plane into areas A and B , such that the dotted line belongs to area B . The Radon planes with lines of intersection in area A are 1-planes. These planes either have only one IP with the helix (the current source position) or the remaining IPs do not belong to the Pi segment, i.e., to $C_{BP}(\mathbf{x})$. Radon planes with intersection lines in area B are 3-planes. The proof given in the sequel consists of different steps. First, we show that 1-planes receive a weight of 1 from the single IP. Second, we argue that for 3-planes, the central IP always contributes with a weight of 1. Finally, we prove that for 3-planes the contributions of the first and third IP cancel.

We begin with some general observations. Remember that line L_1 is the asymptote on the helix. Line L_1 is parallel to $\dot{\mathbf{y}}_H(s)$. We denote the line of intersection of the Radon plane and the planar detector as \mathcal{R} . Now, we argue that projecting \mathbf{x} into the Pi window from the first point of a 3-plane, the point of projection must be above L_1 . Line \mathcal{R} must intersect twice with the $C_{BP}(\mathbf{x})$ -part of the upper Pi-window boundary seen from the first IP (compare with Figure 34). If \mathbf{x} is projected below L_1 , line \mathcal{R} must be steeper than line L_1 in order to have an intersection with the upper Pi-window boundary. Now,

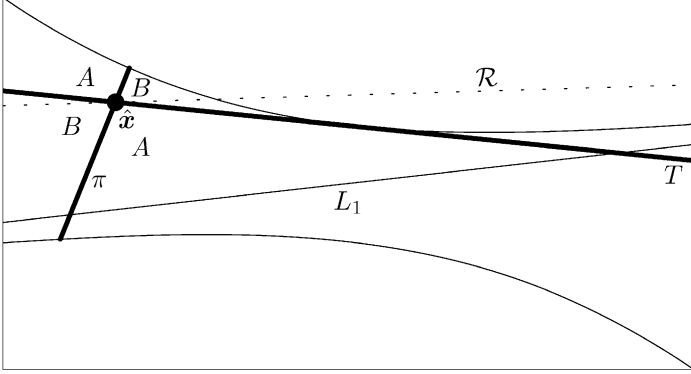


FIGURE 37. The object point is projected onto \hat{x} . The Pi-line (indicated by π) and the tangent on the upper Pi-window boundary (indicated by T) separate the detector plane into areas A and B . The dotted line corresponds to a Radon plane with three IPs with $C_{BP}(x)$.

line \mathcal{R} can have at most one IP with the $C_{BP}(x)$ -part of the upper Pi-window boundary, such that the source position cannot be the first IP, if x is projected below L_1 . Similarly, x must be projected below L_1 from the third IP of a 3-plane. With these observations in mind we realize that the tangential line T in Figure 37 must have a gradient smaller than the gradient of line L_1 .

The arrow in Figure 38 originating from \hat{x} is parallel to $\dot{y}_H(s)$ such that the line that contains \hat{x} and is parallel to the arrow is parallel to L_1 . This line divides area B into areas B_1 and B_2 . Obviously, for Radon planes with intersection lines \mathcal{R} in B_1 , the current source position corresponds to the first IP, whereas for 3-planes with \mathcal{R} in B_2 the current source position is the central IP. We argue that the filter line, which must be used for point \hat{x} , is located in area B_1 . Remember that the corresponding κ -plane has three IPs with $C_{BP}(x)$. If \hat{x} is located above L_1 , the κ -plane has two IPs in the future. In other words, the κ -line must have two IPs with the upper Pi-window boundary. This is only possible if the filter line is located in area B_1 .

Consider the exemplary line \mathcal{R} in Figure 38 located in area B_2 . Once again, we draw $\hat{\omega}$, i.e., the projection of the normal vector of the Radon plane, such that $\text{sgn}(\hat{\omega} \cdot \dot{y}_H) = 1$. Since the filter line is located in B_1 , we realize that also $\text{sgn}(\hat{\omega} \cdot \hat{e}_v) = 1$. This remains true if we rotate the dotted line \mathcal{R} counterclockwise into area A (remember that the gradient of line T is smaller than the gradient of L_1). In other words, the two sgn -functions in Eq. (58) contribute with a factor 1, both for 1-planes (area A) and from the central IP of 3-planes (area B_1). Therefore, all that remains to finish the proof is to show that the contributions of the first and third IPs of a 3-plane cancel when summing over k in Eq. (58).

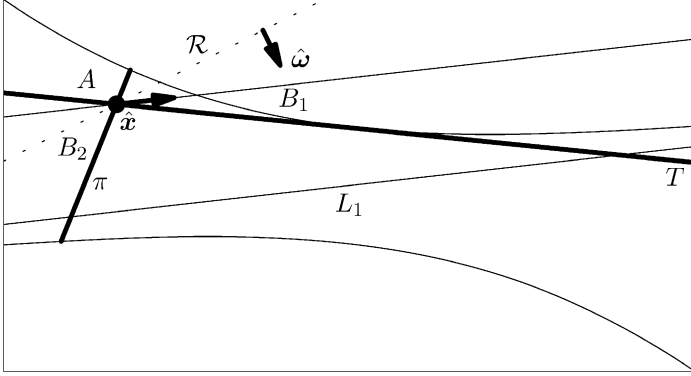


FIGURE 38. The arrow originating from \hat{x} is parallel to $\dot{y}_H(s)$. The line containing \hat{x} and the arrow is parallel to the asymptote on the helix. This line divides area B defined in Figure 37 into areas B_1 and B_2 . The dotted line \mathcal{R} is located in area B_2 . For the 3-plane associated with \mathcal{R} the current focal-spot position is the central IP.

We consider a 3-plane and denote the three IPs as $y_H(s_1)$, $y_H(s_2)$, and $y_H(s_3)$, $s_1 < s_2 < s_3$. Seen from $y_H(s_1)$, the line \mathcal{R} associated with the 3-plane must be located in area B_1 . Moreover, the filter line to be used from $y_H(s_1)$ is also located in area B_1 . We denote the remaining two IPs of the corresponding κ -plane as $y_H(s_{\kappa 1})$ and $y_H(s_{\kappa 2})$. To be precise, we write $s_{\kappa 1}(s_1)$, $s_{\kappa 2}(s_1)$ for the specification of the filter line to be used from $y_H(s_1)$. There are two possibilities for the ordering of the IP, illustrated in Figure 39. The solid lines denoted by κ indicate the filter lines, while the dotted lines correspond to the Radon plane. The two possibilities are treated separately in the following two cases.

Case 1. $s_1 < s_{\kappa 1}(s_1) < s_2 < s_3 < s_{\kappa 2}(s_1)$. This case corresponds to the first image in Figure 39. Obviously, the angles between $\hat{\omega}$ and \dot{y}_H and between $\hat{\omega}$ and \hat{e}_v are less than 90 degrees. Therefore, the two sgn-functions in Eq. (58) contribute with a factor of 1 for the first IP of the Radon plane in this case. With the definition of the κ -planes given above, the central IP of the κ -plane must be located right in the (angular) middle of the other two IPs. Therefore,

$$s_{\kappa 1}(s_1) = \frac{s_{\kappa 2}(s_1) + s_1}{2} < s_2 < s_3 < s_{\kappa 2}(s_1). \quad (101)$$

We now argue that, seen from $y_H(s_3)$, the situation shown in Figure 40 follows, such that $s_1 < s_{\kappa 2}(s_3) < s_{\kappa 1}(s_3) < s_2 < s_3$. Otherwise, $s_{\kappa 2}(s_3) < s_1 < s_2 < s_{\kappa 1}(s_3) = (s_{\kappa 2}(s_3) + s_3)/2$ must be fulfilled. Together with Eq. (101) this leads to $(s_{\kappa 2}(s_1) + s_1)/2 < (s_{\kappa 2}(s_3) + s_3)/2$ and $s_{\kappa 2}(s_3) < s_1 < s_3 < s_{\kappa 2}(s_1)$, which is clearly a contradiction.

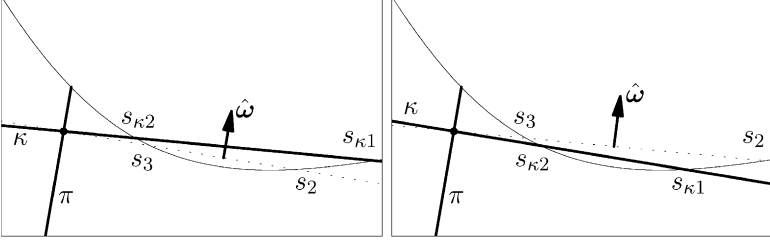


FIGURE 39. Upper half of the planar detector. Considering 3-planes with two IPs in the future, two possibilities exist for the order of IPs. Either $s_1 < s_{\kappa 1} < s_2 < s_3 < s_{\kappa 2}$ or $s_1 < s_2 < s_{\kappa 1} < s_{\kappa 2} < s_3$. For illustration purposes, the shown filter lines κ deviate from the filter lines of the specified algorithm. Nevertheless, the given arguments remain valid.

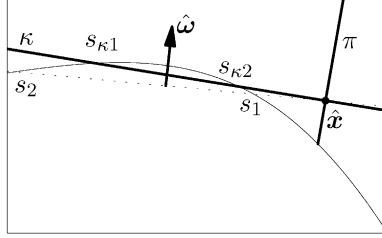


FIGURE 40. The lower half of the planar detector; similar to the first image in Figure 39, seen from the third IP of the 3-plane. Here $s_1 < s_{\kappa 2} < s_{\kappa 1} < s_2 < s_3$.

The angle between $\hat{\omega}$ and \hat{e}_v in Figure 40 is larger than 90 degrees, such that the third IP contributes with a weight of -1 in Eq. (58). In other words, the contributions of the first and the third IPs cancel as desired.

Case 2. $s_1 < s_2 < s_{\kappa 1}(s_1) < s_{\kappa 2}(s_1) < s_3$. This case corresponds to the second image in Figure 39. Now, the first IP contributes with a weight of -1 in Eq. (58). The proof that the third IP now contributes with a positive weight is identical to Case 1.

F. EnPiT: Helical n -Pi Reconstruction

The Pi-method discussed in the previous section suffices for demonstrating exact reconstruction using helical data. Nevertheless, data obtained with a Pi-acquisition have only few redundancies. Therefore, Pi-methods are sensitive to patient motion and might result in noisy data if the tube current is not sufficiently high. Moreover, for given gantry rotation speed and detector

height, the Pi-mode determines the table feed. The latter can reach huge values for modern cone-beam scanners.

The n -Pi mode introduced in Section II.D reduces some of these problems. For an n -Pi acquisition, the table feed is much smaller than for the Pi-mode, and more redundant data are acquired. Redundancies reflect themselves in the type of Radon planes that occur. In the n -Pi case, Radon planes can have $1, 3, \dots, n + 2$ IPs with $C_{BP}(\mathbf{x})$. The backprojection segment, $C_{BP}(\mathbf{x})$, contains all points along the helix from which \mathbf{x} is projected into the n -Pi window. The vast majority of Radon planes has n IPs for typical system parameters. Here we summarize a reconstruction algorithm denoted as $EnPiT$, which was published by Bontus *et al.* (2003, 2005). $EnPiT$ is a quasi-exact reconstruction algorithm in the sense that some n - and $(n + 2)$ -planes receive the incorrect weighting. Nevertheless, reconstruction results show that the approximation is rather good. An exact algorithm for the 3-Pi case was published by Katsevich (2006).

1. Reconstruction Algorithm

The filter-line sets defined below are denoted as $\mathcal{L}_p^{(L)}$ (p odd, $1 \leq p < n$) and $\mathcal{L}_p^{(R)}$ (p odd, $1 \leq p \leq n$). As shown in Bontus *et al.* (2005), these sets provide the following features at least in cases in which no interrupted illumination occurs:

1. A 1-plane gets a positive contribution from each filter-line set.
2. An n -plane gets a positive contribution from set $\mathcal{L}_n^{(R)}$ for each of the n IPs (intersection with $C_{BP}(\mathbf{x})$). The contributions of $\mathcal{L}_p^{(L)}$ and $\mathcal{L}_p^{(R)}$ with $p < n$ cancel.
3. An m -plane, $3 \leq m < n$, gets a positive contribution from $\mathcal{L}_n^{(R)}$ at each of the m IPs, while the contributions of $\mathcal{L}_p^{(L)}$ and $\mathcal{L}_p^{(R)}$ with $p < m$ cancel. For $m \leq p < n$, $\mathcal{L}_p^{(L)}$ and $\mathcal{L}_p^{(R)}$ contribute with a positive weight only to the first and last IPs while the contributions of these sets cancel for the inner IP.

Filter lines of each set $\mathcal{L}_p^{(L)}$ or $\mathcal{L}_p^{(R)}$ are located completely in the p -Pi window. In order to consider all filter lines for an n -Pi reconstruction, we must use all sets $\mathcal{L}_1^{(L)}, \mathcal{L}_3^{(L)}, \dots, \mathcal{L}_{n-2}^{(L)}$ and $\mathcal{L}_1^{(R)}, \mathcal{L}_3^{(R)}, \dots, \mathcal{L}_n^{(R)}$. From every position within the backprojection interval the object point under consideration is projected onto the detector. For the reconstruction, the values of all filter lines, which contain the projection point, must be added using the correct weighting factors μ_v . This means that up to n values must be added, depending on the position of the projection point. We denote the weights for sets $\mathcal{L}_m^{(R)}$ and $\mathcal{L}_m^{(L)}$ as $\mu_m^{(R)}$ and $\mu_m^{(L)}$, respectively. For $n = 3$ all weights are

equal to 1. For $n > 3$ the corresponding values are given by

$$\begin{aligned} n\mu_m^{(R)} &= \begin{cases} \frac{n+1}{4}, & m = 1, \\ \frac{1}{2}, & 3 \leq m \leq n-2, \\ 1, & m = n, \end{cases} \\ -n\mu_m^{(L)} &= \begin{cases} \frac{n+1}{4}, & m = 1, \\ \frac{1}{2}, & 3 \leq m \leq n-2. \end{cases} \end{aligned} \quad (102)$$

These weights have been chosen such that (keeping the features enumerated above in mind) the majority of Radon planes receive the correct weighting. For instance, the second point in the enumeration above tells us that n -planes receive positive contributions only from set $\mathcal{L}_n^{(R)}$. From each of the n IPs the n -plane gets a weight of $1/n$.

2. Filter Lines

To define the different filter lines that are necessary to perform the n -Pi reconstruction we first introduce certain lines, which separate the planar detector into different regions. As above, L_1 is the asymptote of the Pi window. In the same manner, we define the lines L_m and L_{-m} as the lines parallel to L_1 but tangential on the upper and lower m -Pi window boundaries, respectively. Finally, we define the set of lines L_{-p}^m as the lines that have a negative gradient and are both tangential on the upper m -Pi window boundary and on the lower p -Pi window boundary. Figure 41 shows some of these lines within the 5-Pi window.

We define different sets of filter lines and denote these sets as $\mathcal{L}_m^{(L)}$ and $\mathcal{L}_m^{(R)}$ for different values of m . In particular, the corresponding filter line within $\mathcal{L}_m^{(L)}$ for a point $(u_{p\ell}, v_{p\ell})$ within the m -Pi window fulfills the following conditions:

- IF** $(u_{p\ell}, v_{p\ell})$ is above L_{-1}^m , the filter line is tangential on the upper m -Pi window boundary
- ELSE IF** $(u_{p\ell}, v_{p\ell})$ is above L_{-1}^1 , the filter line is tangential on the lower Pi-window boundary
- ELSE IF** $(u_{p\ell}, v_{p\ell})$ is above L_{-m}^1 , the filter line is tangential on the upper Pi-window boundary
- ELSE** the filter line is tangential on the lower m -Pi window boundary.

The corresponding filter line within $\mathcal{L}_m^{(R)}$ for a point $(u_{p\ell}, v_{p\ell})$ within the m -Pi window fulfills the following conditions:

- IF** $(u_{p\ell}, v_{p\ell})$ is above L_m , the filter line is tangential on the upper m -Pi window boundary

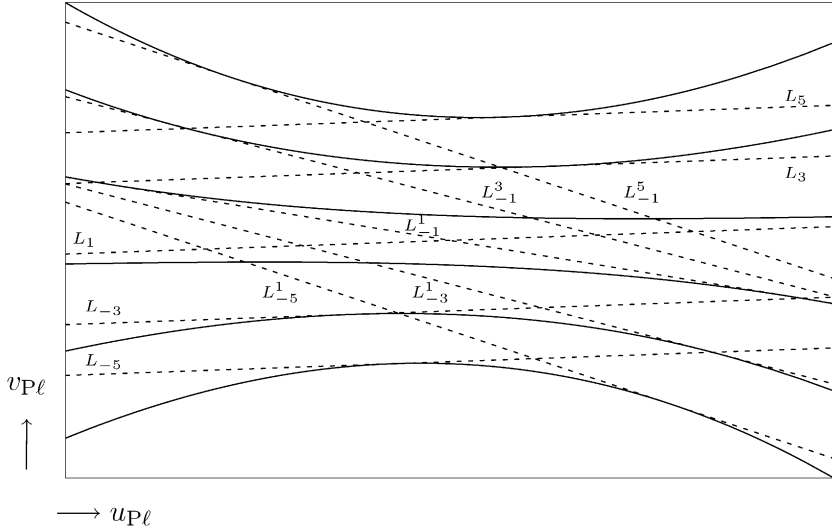


FIGURE 41. Different lines of the sets L_m and L_{-p}^m within the 5-Pi window.

ELSE IF $(u_{P\ell}, v_{P\ell})$ is above L_{-m} , the filter line is parallel to L_1

ELSE the filter line is tangential on the lower m -Pi window boundary.

Obviously, any filter line is either tangential on one of the p -Pi window boundaries or parallel to $\dot{\mathbf{y}}_H(s)$. For the definitions of the tangents, we still have to say, whether the point of tangency is on the left-hand side (LHS) or the right-hand side (RHS) of $(u_{P\ell}, v_{P\ell})$. In general, for filter lines within $\mathcal{L}_m^{(L)}$, the point of tangency is on the LHS of $(u_{P\ell}, v_{P\ell})$ if the line is tangential on one of the upper p -Pi window boundaries, while it is on the RHS, if the line is tangential on one of the lower p -Pi window boundaries. For those lines within $\mathcal{L}_m^{(R)}$ that are tangential on the m -Pi window boundary, we must consider the point at which L_m is tangential on the m -Pi window boundary. If $(u_{P\ell}, v_{P\ell})$ is located left of this point, the point of tangency is on the RHS of $(u_{P\ell}, v_{P\ell})$; if $(u_{P\ell}, v_{P\ell})$ is located right of this point, the point of tangency is on the LHS of $(u_{P\ell}, v_{P\ell})$. Figures 42 and 43 show the filter lines for the 5-Pi case.

G. CEnPiT: Helical Cardiac CT

1. Cardiac CT

Cardiac CT is one important application of CT. Due to the beating heart cardiac CT is challenging with respect to image quality and temporal resolution. We restrict this application to a discussion of cardiac CT based on a helical

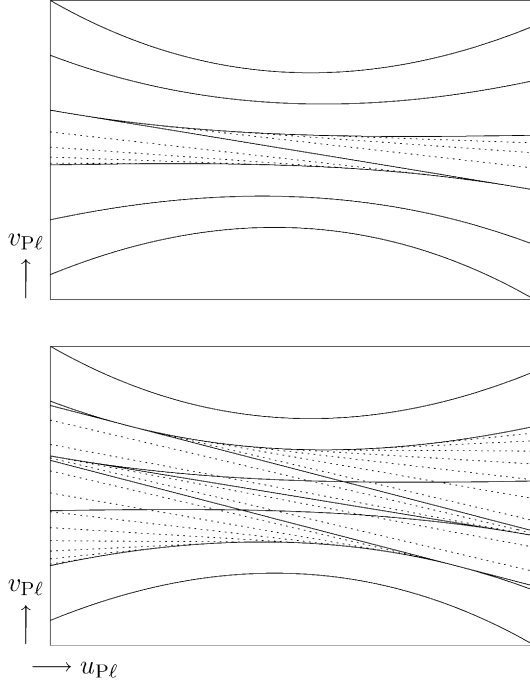


FIGURE 42. 5-Pi filter lines; from top to bottom: $\mathcal{L}_1^{(L)}$ and $\mathcal{L}_3^{(L)}$.

acquisition. In particular, we assume that the data were obtained with a low-pitch helix, which can be associated with an n -Pi acquisition. Typical values of n are 9 or 11.

Cardiac CT data usually are acquired simultaneously with the electrocardiogram (ECG). The aim of reconstruction is to obtain images associated with a certain motion state of the heart, and the ECG data are related to the motion states. R peaks are the canonical markers to describe the cardiac cycle based on the ECG. The cardiac cycle is considered to reach from one R peak to the next. States of the cardiac cycle are described based on these intervals. For instance, a phase point of 70% specifies that all time points are considered that are located at $t = t_0 + 0.7\Delta t$. Here Δt is the time period between the R peak at t_0 and its successor (see Figure 44). The situation becomes more difficult since the phase point in which the heart is in the state of least motion varies from patient to patient. Motion maps (Manzke *et al.*, 2004) yield good results for finding the phase points of least motion. In the following discussion, we assume that the phase point at which the reconstruction shall be performed is known.

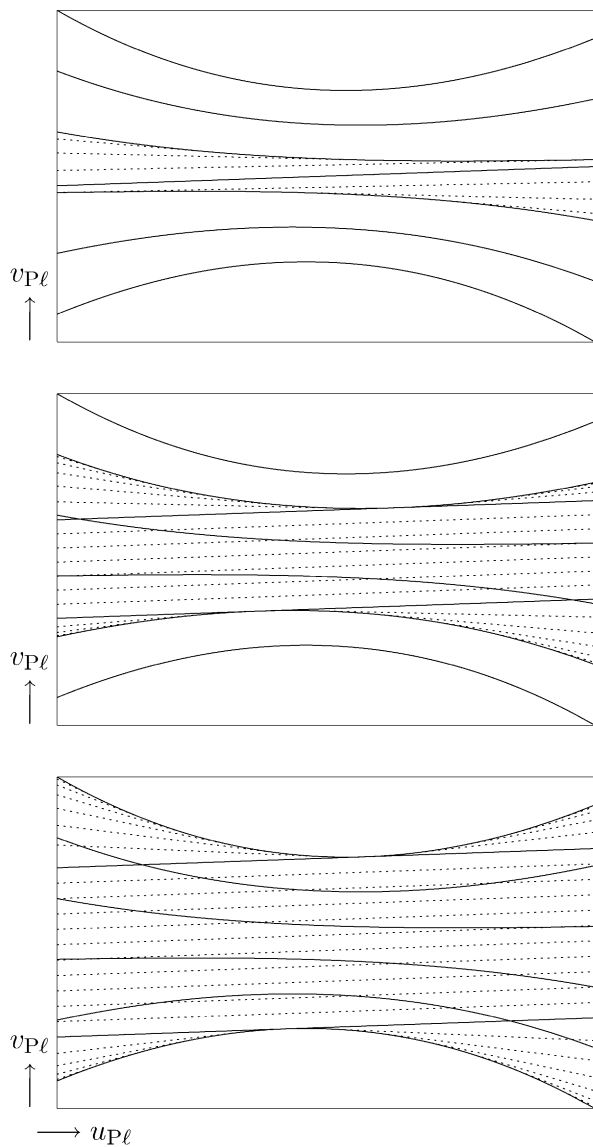


FIGURE 43. 5-Pi filter lines. From top to bottom: $\mathcal{L}_1^{(R)}$, $\mathcal{L}_3^{(R)}$, and $\mathcal{L}_5^{(R)}$.

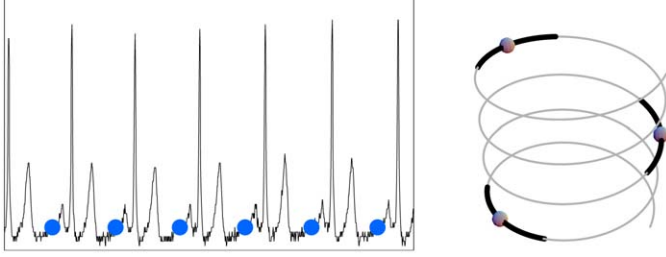


FIGURE 44. The highlighted points on the ECG correspond to the phase points. The phase points are specified relative to the R peaks. Each phase point is associated with a certain point on the helix. The amount of data used for reconstruction around each phase point define the width of the gating window.

A simple *EnPiT* reconstruction cannot yield good cardiac images. Cardiac CT requires to use of data acquired at time points close to the phase points, while data at a large temporal distance to the phase points should be neglected. A good reconstruction algorithm therefore must exploit the given redundancies. Redundancies reflect themselves in the different types of Radon planes for the kinds of reconstruction algorithms discussed here. Certainly for 1-planes there is no redundancy. Fortunately, the majority of Radon planes has n IPs and Radon planes with fewer IPs contribute mainly to the low-frequency components of the images (compare with Section III.A.2). The *CEnPiT* algorithm, published first in [Bontus et al. \(2006\)](#), exploits these facts. Moreover, *CEnPiT* uses data of the *complete* focus detector—it is not restricted to the n -Pi window. The latter fact is important for obtaining the optimal temporal resolution and the best SNR in all cases.

Reconstruction algorithms are called *gated algorithms* if they assign weights to the projections and if the weights depend on the distance of the projection to the phase point. The *CEnPiT* approach separates the data into two contributions, μ^{ug} and μ^{g} , which are added to result in the final image. In particular, μ^{ug} contains contributions of Radon planes with up to n IPs, while μ^{g} contains contributions of Radon planes with more than n IPs. With discussion in mind, we realize that μ^{ug} yields mainly low-frequency components. Together with the fact that μ^{ug} contains Radon planes with only few redundancies, we are motivated to use an ungated backprojection when computing μ^{ug} . Gating is applied only to obtain μ^{g} . For the possibilities to choose an adequate gating function we refer to [Bontus et al. \(2006\)](#). Here we summarize the filter-line sets, which can be used to separate the data into μ^{ug} and μ^{g} .

2. Filter Lines

The filter lines summarized here were first published by Köhler, Bontus and Koken (2006). The topic was discussed on an even wider basis in Köhler, Bontus and Koken (2006), where the results were used to incorporate overscan data. Overscan data correspond to measured data outside of the n -Pi window. The different kinds of filter-line sets are denoted as $\mathcal{L}_m^{(R)}$, $\mathcal{P}_m^{(L)}$, $\mathcal{P}_m^{(R)}$, and $\mathcal{T}^{(R)}$, where m can be any positive odd integer. The definition for sets $\mathcal{L}_m^{(R)}$ has been given in Section III.F. For the definition of the remaining sets, we introduce helper lines L_p^m and L_{\pm}^F in addition to lines L_m , L_{-m} , and L_{-p}^m introduced in Section III.F (compare with Figure 41). In particular, line L_p^m has a positive gradient and is tangential on the upper m -Pi window and on the lower p -Pi window. Lines L_{\pm}^F are parallel to L_1 and tangential on the projected boundaries of the focus detector [compare with Eq. (33)]. Figure 45 shows some of these helper lines.

The definition of filter-line set $\mathcal{T}^{(R)}$ is similar to that of sets $\mathcal{L}_m^{(R)}$. Filter lines within $\mathcal{T}^{(R)}$ are parallel to L_1 , if $(u_{p\ell}, v_{p\ell})$ is located between L_-^F and L_+^F . Otherwise, the filter lines are tangential on the projected focus-detector borders [cf. Eq. (33)]. Figure 46 shows the filter-line set $\mathcal{T}^{(R)}$. The filter lines $\mathcal{P}_m^{(L)}$ and $\mathcal{P}_m^{(R)}$ are completely contained within the m -Pi window. In particular, the corresponding filter line within $\mathcal{P}_m^{(R)}$ for a point $(u_{p\ell}, v_{p\ell})$ within the m -Pi window fulfills the following conditions:

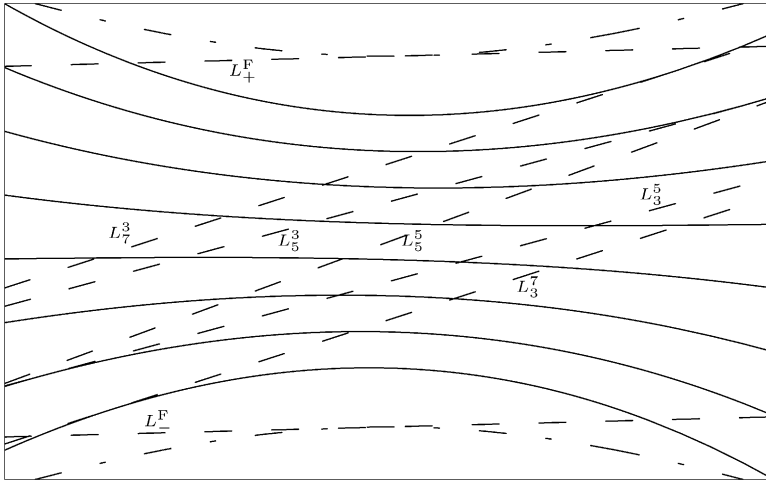
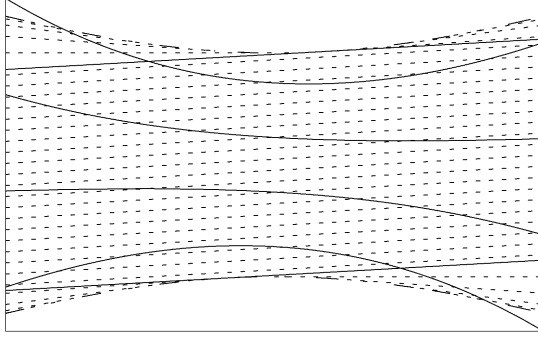


FIGURE 45. Different lines of set \mathcal{L}_p^m and lines L_{\pm}^F within the 7-Pi window. The dash-dotted lines correspond to the projections of the focus-detector boundaries [Eq. (33)].

FIGURE 46. Filter-line set $\mathcal{T}^{(R)}$.

- IF** $(u_{p\ell}, v_{p\ell})$ is above L_3^m , the filter line is tangential on the upper m -Pi window boundary
ELSE IF $(u_{p\ell}, v_{p\ell})$ is above L_3^{m-2} , the filter line is tangential on the lower 3-Pi window boundary
ELSE IF $(u_{p\ell}, v_{p\ell})$ is above L_5^{m-2} , the filter line is tangential on the upper $(m - 2)$ -Pi window boundary
ELSE IF $(u_{p\ell}, v_{p\ell})$ is above L_5^{m-4} , the filter line is tangential on the lower 5-Pi window boundary
 ...
ELSE IF $(u_{p\ell}, v_{p\ell})$ is above L_m^3 , the filter line is tangential on the upper 3-Pi window boundary
ELSE the filter line is tangential on the lower m -Pi window boundary.

The corresponding filter line within $\mathcal{P}_m^{(L)}$ for a point $(u_{p\ell}, v_{p\ell})$ within the m -Pi window fulfills the following conditions:

- IF** $(u_{p\ell}, v_{p\ell})$ is above L_{-1}^m , the filter line is tangential on the upper m -Pi window boundary
ELSE IF $(u_{p\ell}, v_{p\ell})$ is above L_{-1}^{m-2} , the filter line is tangential on the lower Pi-window boundary
ELSE IF $(u_{p\ell}, v_{p\ell})$ is above L_{-3}^{m-2} , the filter line is tangential on the upper $(m - 2)$ -Pi window boundary
ELSE IF $(u_{p\ell}, v_{p\ell})$ is above L_{-3}^{m-4} , the filter line is tangential on the lower 3-Pi window boundary
 ...
ELSE IF $(u_{p\ell}, v_{p\ell})$ is above L_{-m}^1 , the filter line is tangential on the upper Pi-window boundary
ELSE the filter line is tangential on the lower m -Pi window boundary.

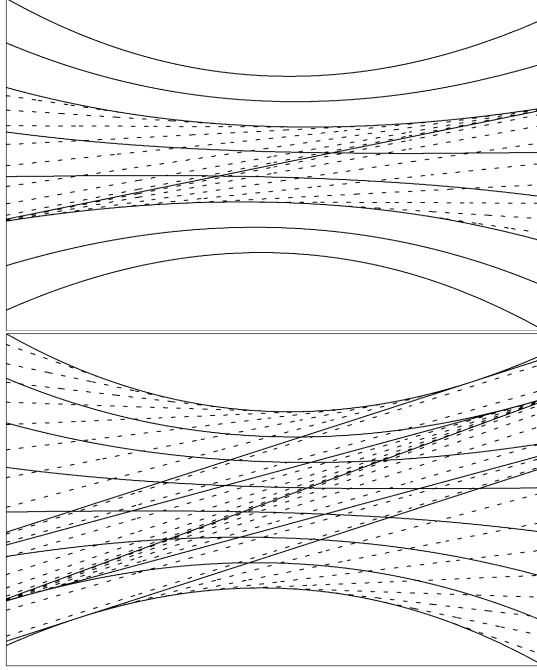
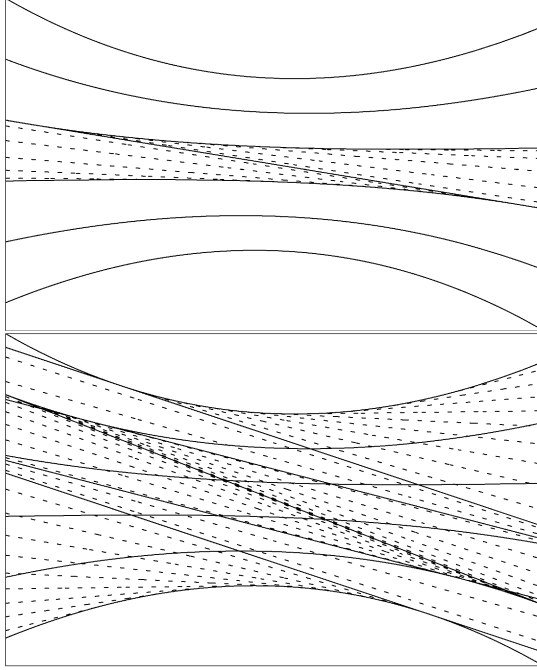


FIGURE 47. Filter-line sets $\mathcal{P}_3^{(R)}$ and $\mathcal{P}_7^{(R)}$.

We still must specify whether the point of tangency is on the RHS or LHS of $(u_{\text{Pl}}, v_{\text{Pl}})$. In general, for filter lines within $\mathcal{P}_m^{(L)}$, the point of tangency is on the LHS of $(u_{\text{Pl}}, v_{\text{Pl}})$, if the line is tangential on one of the upper p -Pi window boundaries, while it is on the RHS, if the line is tangential on one of the lower p -Pi-window boundaries. For filter lines within $\mathcal{P}_m^{(R)}$, the point of tangency is on the RHS of $(u_{\text{Pl}}, v_{\text{Pl}})$, if the line is tangential on one of the upper p -Pi window boundaries, while it is on the LHS, if the line is tangential on one of the lower p -Pi window boundaries. Figure 47 exemplifies sets $\mathcal{P}_3^{(R)}$ and $\mathcal{P}_7^{(R)}$, while Figure 48 illustrates sets $\mathcal{P}_1^{(L)}$ and $\mathcal{P}_5^{(L)}$.

3. Gated and Ungated Contributions

With the definitions of the filter lines we can now specify how the gated and ungated contributions μ^g and μ^{ug} are obtained. We assume that n specifies the maximum Pi-mode; i.e. the n -Pi window can be projected completely onto the focus detector, while the $(n + 2)$ -Pi window cannot. With this convention the filter-line sets and weights μ_v for μ^{ug} are summarized in Table 2. The

FIGURE 48. Filter-line sets $\mathcal{P}_1^{(L)}$ and $\mathcal{P}_5^{(L)}$.

contributions of all those filter-line sets must be added. For instance, line 2 in Table 2 shows that sets $\mathcal{L}_3^{(R)}, \mathcal{L}_5^{(R)}, \dots, \mathcal{L}_{n-2}^{(R)}$ must be incorporated using the specified weights. Table 3 summarizes the filter-line sets and weights for μ^g .

IV. OUTLOOK

The publication of Katsevich's Pi algorithm initiated many studies. It even resulted in new insights on fan-beam CT (Noo, Clackdoyle and Pack, 2004). We have summarized the principles and showed some applications of the methods. A more detailed analysis of the underlying mathematics was given by Chen (2003), Katsevich (2003). In practice, a utilization of all measured data is desired. A restriction to the n -Pi window in the case of helical CT is not acceptable for clinical applications. Köhler, Bontus and Koken (2006) showed how *overscan data* can be incorporated in the reconstruction. A nice FBP algorithm for the saddle trajectory was presented by Yang *et al.* (2006). Future applications could require algorithms for helical CT with

TABLE 2
FILTER-LINE SETS AND THE
CORRESPONDING WEIGHTS FOR μ^{ug}

Filter-line sets	$n\mu_v$
$\mathcal{L}_1^{(R)}$	$\frac{n}{3}$
$\mathcal{L}_p^{(R)}, 3 \leq p < n$	$\frac{2n}{p(p+2)}$
$\mathcal{L}_n^{(R)}$	1
$\mathcal{P}_1^{(L)}$	$-\frac{n}{3}$
$\mathcal{P}_p^{(L)}, 3 \leq p < n$	$-\frac{n}{p(p+2)}$
$\mathcal{P}_n^{(L)}$	$-\frac{1}{2}$
$\mathcal{P}_p^{(R)}, 3 \leq p < n$	$\frac{-n}{p(p+2)}$
$\mathcal{P}_n^{(R)}$	$-\frac{1}{2}$

TABLE 3
FILTER-LINE SETS AND THE
CORRESPONDING WEIGHTS FOR μ^{g}

Filter-line sets	$n\mu_v$
$\mathcal{L}_n^{(R)}$	$-\frac{n}{n+2}$
$\mathcal{P}_n^{(L)}$	$\frac{n}{2(n+2)}$
$\mathcal{P}_n^{(R)}$	$\frac{n}{2(n+2)}$
$\mathcal{T}^{(R)}$	$\frac{n}{n+2}$

a tilted gantry (Noo, Defrise and Kudo, 2004) or for acquisitions in which the table feed (pitch) is not constant (Katsevich, Basu and Hsieh, 2004; Ye, Zhu and Wang, 2004).

Circular CT becomes increasingly attractive with greater numbers of detector rows. This is especially true if the organ under examination is completely covered by the X-ray cone. As discussed previously, a circular cone-beam acquisition yields an incomplete data set. The combination of the circle with a line provides one way to restore completeness as shown in Section III.D. Alternatively, the circle can also be combined with a helical segment (Bontus *et al.*, 2007a, 2007b). The advantage of this approach is that the gantry need not be decelerated or accelerated, while the helical segment contributes only to low-frequency components in the same sense as the line does in the CLT.

A completely new class of reconstruction algorithms appeared by exploitation of a formula derived by Zou and Pan (2004a). The authors derived two reconstruction algorithms for which the data must be filtered either in the image domain (Zou and Pan, 2004a) (backprojection filtering, BPF) or along projected Pi-lines (Zou and Pan, 2004b) (filtered backprojection, FBP). Another BPF formula was derived by Zhuang *et al.* (2004), which can be applied to different kinds of source trajectories. BPF algorithms apply a backprojection to data, that are only differentiated along the tangent of the trajectory [as in Eq. (43)]. The result corresponds to image data modified by a Hilbert transform. Therefore, an inverse Hilbert transform must be applied as one of the final processing steps. Pack, Noo and Clackdoyle (2005) presented a BPF method that can be used for different source trajectories and allows use of an arbitrary amount of overscan data during the backprojection.

Nevertheless, with this method a large number of processing steps can become necessary to obtain an adequate SNR.

CT reconstruction is an interesting and agile field of research. The future will show which of the proposed algorithms fulfill the requirements imposed by clinical practice.

REFERENCES

- Bontus, C., Köhler, T., Proksa, R. (2003). A quasiaexact reconstruction algorithm for helical CT using a 3-Pi acquisition. *Med. Phys.* **30** (9), 2493–2502.
- Bontus, C., Köhler, T., Proksa, R. (2005). EnPiT: Filtered back-projection algorithm for helical CT using an n -Pi acquisition. *IEEE Trans. Med. Imaging* **24** (8), 977–986.
- Bontus, C., Koken, P., Köhler, T., Grass, M. (2006). CEnPiT: Helical cardiac CT reconstruction. *Med. Phys.* **33** (8), 2792–2799.
- Bontus, C., Grass, M., Koken, P., Köhler, T. (2007a). Exact reconstruction algorithm for circular short-scan CT combined with a helical segment. In: *Proceedings of the Fully 3D Meeting*. Lindau, Germany, pp. 88–91.
- Bontus, C., Koken, P., Köhler, T., Proksa, R. (2007b). Circular CT in combination with a helical segment. *Phys. Med. Biol.* **52**, 107–120.
- Chen, G.-H. (2003). An alternative derivation of Katsevich's cone-beam reconstruction formula. *Med. Phys.* **30** (12), 3217–3225.
- Danielsson, P.E., Edholm, P., Eriksson, J., Magnusson-Seger, M. (1997). Towards exact 3D-reconstruction for helical cone-beam scanning of long objects. In: *Proceedings of the 3D'97 Conference*. Nemacon, Pennsylvania, pp. 141–144.
- Defrise, M., Noo, F., Kudo, H. (2000). A solution to the long object problem in helical cone-beam tomography. *Phys. Med. Biol.* **45**, 623–643.
- Grangeat, P. (1991). *Mathematical Framework of Cone-Beam 3D-Reconstruction via the First Derivative of the Radon Transformation*. *Mathematical Methods in Tomography*. Springer, Berlin, Germany.
- Jeffrey, A., Gradshteyn, I.S., Ryzhik, I.M. (Eds.) (1994). *Table of Integrals, Series, and Products*, fifth edition. Academic Press, San Diego.
- Katsevich, A. (2002). Theoretically exact FBP-type inversion algorithm for spiral CT. *SIAM J. Appl. Math.* **62**, 2012–2026.
- Katsevich, A. (2003). A general scheme for constructing inversion algorithms for cone beam CT. *Int. J. Math. Math. Sci.* **21**, 1305–1321.
- Katsevich, A. (2004a). Image reconstruction for the circle and line trajectory. *Phys. Med. Biol.* **49**, 5059–5072.
- Katsevich, A. (2004b). An improved exact FBP algorithm for spiral CT. *Adv. Appl. Math.* **32** (4), 681–697.

- Katsevich, A. (2006). 3PI algorithms for helical computed tomography. *Adv. Appl. Math.* **36**, 213–250.
- Katsevich, A., Basu, S., Hsieh, J. (2004). Exact filtered backprojection reconstruction for dynamic pitch helical cone beam computed tomography. *Phys. Med. Biol.* **49**, 3089–3103.
- Köhler, T., Bontus, C., Koken, P. (2006). The Radon-split method for helical cone-beam CT and its application to nongated reconstruction. *IEEE Trans. Med. Imaging* **25** (7), 882–897.
- Kudo, H., Noo, F., Defrise, M. (1998). Cone-beam filtered-backprojection algorithm for truncated helical data. *Phys. Med. Biol.* **43**, 2885–2909.
- Manzke, R., Köhler, T., Nielsen, T., Hawkes, D., Grass, M. (2004). Automatic phase determination for retrospectively gated cardiac CT. *Med. Phys.* **31** (12), 3345–3362.
- Natterer, F. (1986). *The Mathematics of Computerized Tomography*. Wiley, New York.
- Noo, F., Clackdoyle, R., Pack, J. (2004). A two-step Hilbert transform method for 2D image reconstruction. *Phys. Med. Biol.* **49**, 3903–3923.
- Noo, F., Defrise, M., Kudo, H. (2004). General reconstruction theory for multi-slice x-ray computed tomography with a gantry tilt. *IEEE Trans. Med. Imaging* **43** (9), 1109–1116.
- Noo, F., Pack, J., Heuscher, D. (2003). Exact helical reconstruction using native cone-beam geometries. *Phys. Med. Biol.* **48**, 3787–3818.
- Pack, J.D., Noo, F., Clackdoyle, R. (2005). Cone-beam reconstruction using the backprojection of locally filtered projections. *IEEE Trans. Med. Imaging* **24** (1), 70–85.
- Proksa, R., Köhler, T., Grass, M., Timmer, J. (2000). The n -PI-method for helical cone-beam CT. *IEEE Trans. Med. Imaging* **19** (9), 848–863.
- Schaller, S., Noo, F., Sauer, F., Tam, K.C., Lauritsch, G., Flohr, T. (2000). Exact Radon rebinning algorithm for the long object problem in helical cone-beam CT. *IEEE Trans. Med. Imaging* **19** (5), 361–375.
- Tam, K.C. (1995). Three-dimensional computerized tomography scanning method and system for large objects with smaller area detectors. US Patent 5,390,112.
- Tam, K.C., Sauer, F., Lauritsch, G., Steinmetz, A. (1999). Backprojection spiral scan region-of-interest cone beam CT. *Proc. SPIE Med. Imaging Conf.* **3661**, 433–441.
- Tuy, H.K. (1983). An inversion formula for cone-beam reconstructions. *SIAM J. Appl. Math.* **43** (3), 546–552.
- Yang, H., Li, M., Koizumi, K., Kudo, H. (2006). View-independent reconstruction algorithms for cone beam CT with general saddle trajectory. *Phys. Med. Biol.* **51**, 3865–3884.

- Ye, Y., Zhu, J., Wang, G. (2004). Minimum detection windows, PI-line existence and uniqueness for helical cone-beam scanning of variable pitch. *Med. Phys.* **31** (3), 566–572.
- Zhuang, T., Leng, S., Nett, B.E., Chen, G. (2004). Fan-beam and cone-beam image reconstruction via filtering the backprojection image of differentiated projection data. *Phys. Med. Biol.* **49**, 5489–5503.
- Zou, Y., Pan, X. (2004a). Exact image reconstruction on PI-lines from minimum data in helical cone-beam CT. *Phys. Med. Biol.* **49**, 941–959.
- Zou, Y., Pan, X. (2004b). Image reconstruction on PI-lines by use of filtered backprojection in helical cone-beam CT. *Phys. Med. Biol.* **49**, 2717–2731.